OIL SPILL DETECTION AND MAPPING ALONG THE GULF OF MEXICO COASTLINE BASED ON IMAGING SPECTROMETER DATA

A Thesis

by

MERYEM DAMLA ARSLAN

Submitted to the Office of Graduate and Professional Studies of
Texas A&M University
in partial fulfillment of the requirements for the degree of

MASTER OF SCIENCE

Chair of Committee,	Anthony M. Filippi
Committee Members,	İnci Güneralp
	Rusty A. Feagin
Head of Department,	Vatche Tchakerian

December 2013

Major Subject: Geography

ABSTRACT

The Deepwater Horizon oil spill in the Gulf of Mexico between April and July 2010 demonstrated the importance of synoptic oil-spill monitoring in coastal environments via remote-sensing methods. This study focuses on terrestrial oil-spill detection based on hyperspectral images acquired along the coastline of the Gulf of Mexico. A number of AVIRIS (Airborne Visible/Infrared Imaging Spectrometer) imaging spectrometer images were investigated in this research collected over Bay Jimmy and Wilkinson Bay within Barataria Bay, Louisiana, USA during September 2010.

Various remote-sensing image processing techniques were employed to detect/identify oiled vegetation. Image-derived endmembers were extracted from the atmospherically- and geometrically-corrected hyperspectral AVIRIS data via Minimum Noise Fraction transform, Pixel Purity Index generation, and *n*-dimensional visualization. Extracted endmembers are then used as input to endmember-mapping algorithms Spectral Information Divergence (SID) and Mixture Tuned Matched Filtering (MTMF) to yield fractional-abundance images and crisp classification images. Field-

based observations of the degree of oil accumulation along the coastline were also employed, as well as *in situ* measurements from the literature.

Multiple Endmember Spectral Mixture Analysis (MESMA) was employed for oiled-vegetation detection and mapping in order to enable the number and types of endmembers to vary on a per-pixel basis, in contrast to simple Spectral Mixture Analysis (SMA). MESMA thus better allows accounting for spectral variability of oil (e.g., due to varying oil thicknesses, states of degradation, and the presence of different oil types, etc.) and other materials, including soils and salt marsh vegetation of varying types, which may or may not be affected by the oil spill. The classification results demonstrated that MESMA provides advantageous capabilities for mapping several oiled-vegetation classes along the Gulf of Mexico coastline, relative to the conventional approaches tested.

DEDICATION

I wish to dedicate this thesis to my mother,

Ayse Arslan

ACKNOWLEDGEMENTS

I take this opportunity to express my sincere appreciation and gratitude to my committee chair, Dr. Anthony M. Filippi, for his invaluable guidance and support through my academic life at Texas A&M University. I deeply appreciate his expertise, professionalism, and commitment to me as his student. Special thanks to Dr. İnci Güneralp for her friendship, considerable support and encouragement throughout my thesis work, and for her useful comments. I also sincerely thank my committee member, Dr. Rusty Feagin for his suggestions and reviews throughout the research and preparation of this thesis.

I gratefully acknowledge the funding I received during my graduate work from the Turkish Petroleum Corporation (TPAO).

I would also like to acknowledge the Jet Propulsion Laboratory, California Institute of Technology for providing airborne imaging spectrometer data of the Gulf of Mexico for this research.

I also want to thank my all colleagues and friends in College Station for their friendship during my stay in College Station.

Thanks to Senih Baydar for being with me from the beginning to the end of this experience and making my life happy and joyful in the United States. Without his support this thesis would not have been possible.

Finally, I would like to express my deep love and appreciation to my mother, Ayse Arslan, my father, Ali Arslan, and my sisters, Elvan Arslan Bayhan, Ismihan

Karadayi and Deniz Arslan, for always believing in me, for their love and encouragement.

NOMENCLATURE

AVIRIS	Airborne Visible/Infrared Imaging Spectrometer
DWH	Deepwater Horizon
DOC	Dissolved Organic Carbon
EEA	Endmember Extraction Algorithm
ENVI™	ENvironment for Visualizing Images™
FLAASH	Fast Line-of-Sight Atmospheric Analysis of Spectral Hypercubes
GOM	Gulf of Mexico
JPL	Jet Propulsion Laboratory
km	kilometer
μm	Micrometer
MESMA	Multiple Endmember Spectral Mixture Analysis
MODTRAN	MODerate resolution atmospheric TRANsmission model
MNF	Minimum Noise Fraction Transformation
MTMF	Mixture Tuned Matched Filtering
NASA	National Aeronautics and Space Administration
nm	Nanometer
NIR	Near Infrared (700-1300 nm)
NOAA	National Oceanic and Atmospheric Administration
PPI	Pixel Purity Index
SAR	Synthetic Aperture RADAR

SCAT	Shoreline Cleanup and Assessment Technique
SID	Spectral Information Divergence
SMA	Spectral Mixture Analysis
SWIR	Shortwave Infrared (1300-2500 nm)
UV	Ultraviolet
VIPER	Visualization and Image Processing for Environmental Research
VNIR/SWIR	Visible/Near Infrared/Shortwave Infrared (400-2500 nm)

TABLE OF CONTENTS

Page

LIST OF FIGURES

Page

LIST OF TABLES

Page

CHAPTER I

INTRODUCTION

The Gulf of Mexico is one of the largest petroleum basins in the world (Galloway, 2009), located adjacent to the landmasses of the continental United States and Mexico. Therefore, given its oil fields, it plays an important role for the petroleum industry and the worldwide economy. Oil spills other than those associated with natural seeps have been occurring offshore during extraction and transportation of oil from offshore sources. In the course of oil and gas exploration and production in Gulf of Mexico, the Deepwater Horizon oil rig accident occurred between 20 April and 15 July 2010, and it is recorded as the largest accidental marine oil spill in history of the petroleum industry, and approximately 200 million gallons crude oil was released into the Gulf of Mexico over the course of 87 days (Crone and Tolstoy, 2010) and resulted in extensive damage to human livelihoods and ecosystems. The spill oiled more than 1000 miles (1600 km) of shoreline along the Gulf of Mexico and even a year later, more than 500 miles (800 km) of shoreline was impacted by tar balls and/or light oiling (NOAA, 2011). This oil-spill incident in the Gulf of Mexico demonstrated the importance of synoptic oil-spill monitoring in coastal environments via remote-sensing methods. Such monitoring can help to minimize the effects of oil spills by facilitating mapping the size, position, and landfall of spills along the coastline. Remote-sensing technology enables oil-spill observation over wide marine and terrestrial areas and can provide data at relatively low cost in comparison to *in situ*-based site observations. Various sensor types

offer differing capabilities for detecting/estimating oil on water and land. This research focuses on hyperspectral remote-sensing image analysis for oil detection along the Gulf of Mexico coastline. Hyperspectral remote sensing, also known as imaging spectroscopy, affords the potential for detailed identification of materials and better estimates of their abundances, relative to multispectral remote sensing (Salem *et al.*, 2001). Hyperspectral sensing often involves recording more than 200 wavelengths of reflected and emitted energy (e.g., Green *et al.*, 1998). Therefore, spectral signatures of various types/states of oil can thus potentially be exploited with the use of hyperspectral image analysis. Extensive previous oil spill remote-sensing research has been conducted in open-ocean and coastal waters. The present research, however, aims to detect/map oil in coastal marsh vegetation areas based on hyperspectral image-derived endmembers. In particular, AVIRIS (Airborne Visible/Infrared Imaging Spectrometer) data (Green *et al.*, 1998) are employed in this research, which represents a well-calibrated image data source that can be utilized for rigorous application to detection of oiled vegetation in this context. This study therefore involves classification of hyperspectral AVIRIS image data to detect oiled vegetation along the Gulf of Mexico coastline, including along tidal channels, observed near the time frame of the Deepwater Horizon oil spill.

1.1 Study Site

The northern Gulf of Mexico basin is one of the world's most active areas of petroleum exploration. Thus, there are thousands oil exploration rigs operating in this area. The Deepwater Horizon drilling platform exploded in the Gulf of Mexico 48 miles off the coast of Louisiana. Since the platform was located 210 km south east of New Orleans and less than 100 km from the Mississippi River delta, very large amount of oil from the Deepwater Horizon accident reached the Louisiana's coast (Figure 1). This spill contaminated over 650 miles of coastal habitat centered primarily on Louisiana's sensitive delta (National Commission 2011).

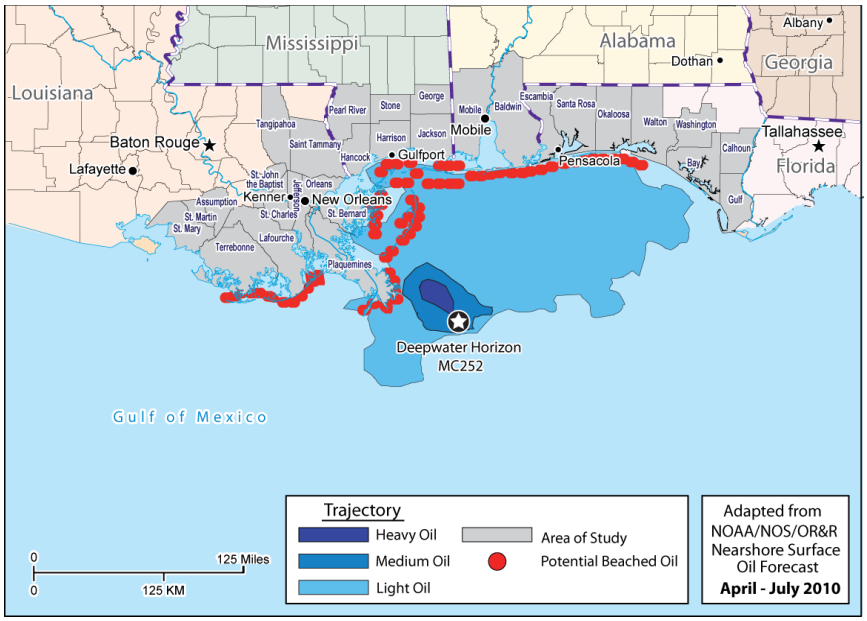

Figure 1 Areas potentially affected by the Deepwater Horizon accident, April-July 2010 (Niehaus, 2010).

Therefore Louisiana's coast was the most heavily impacted area and Barataria Bay estuary in Louisiana was among the most heavily oil impacted coastal embayments. The project area covers the marshes specifically along the coastline of the Bay Jimmy, Wilkinson Bay, and Bay Chene Fleur within the Barataria Bay (Figure 2) in order to identify and map oiled vegetation and create an oil distribution map via analysis of AVIRIS image data. Barataria Basin encompasses an area of approximately 5,720 km^2 of open water and wetland areas, with vegetation mostly dominated by the saline marshes. Salt marshes generally entail more oil-sensitive vegetation than freshwater marshes, and the oil impact on vegetation is most significant in highly organic soils of salt marshes (Lin & Mendelssohn, 1996; Pezeshki *et al.*, 2000).

Figure 2 Map showing the study area, which covers Bay Jimmy, Bay Chene Fleur, and Wilkinson Bay, LA, USA (Image source: ESRI ArcGIS online World Imagery).

1.2 Objectives

In this research, a spectroscopic approach is used to detect oiled vegetation along the Gulf of Mexico in southern Louisiana. The first objective of the thesis research is to map oiled marsh vegetation observed near the time frame of the 2010 Deepwater Horizon (DWH) oil spill along the coastline based on hyperspectral NASA/Jet Propulsion Laboratory AVIRIS image data collected over Barataria Bay, Louisiana, USA with SID and MTMF endmember based hyperspectral classification methods. The second objective of this research is to map oiled marsh vegetation over the same study site by performing MESMA, developed by Roberts *et al.* (1998), which differs from SID and MTMF in terms of the capability of testing multiple endmembers combinations and endmember spectra for each pixel in the image. Given the advantage of MESMA over SID and MTMF, the overall objective of this research is to evaluate the performance three different endmember-based hyperspectral mapping methods in detection of oiled marsh vegetation by performing accuracy assessments. In particular, it will be determined whether significant differences in classification accuracies exist among the results generated by these algorithms. This study focuses on terrestrial oil spill detection, and multiple classification methods will be used to detect oil spills along the coastline of the Gulf of Mexico and adjacent wetland. The primary research question of this study is "Can coastal oil spills be detected and accurately mapped in marsh vegetation and along the coastline of the Gulf of Mexico with the application of hyperspectral image analyses?" This study is innovative because provides an extensive comparative analysis

of the efficacies of several important types of hyperspectral mapping methods, specifically applied to the problem of oiled vegetation detection based on NASA/Jet Propulsion Laboratory AVIRIS image analysis. This research contributes to growing literature in remote sensing and oil-detection analysis using hyperspectral AVIRIS image data. Since the DWH oil spill is currently the largest accidental marine oil spill in history, this review is set within the context of the DWH blowout in 2010, during which approximately 200 million gallons of South Louisiana crude oil was released into the Gulf of Mexico (Crone and Tolstoy, 2010). This spill contaminated over 650 miles of coastal habitat centered primarily on Louisiana's sensitive delta (National Commission, 2011).

1.3 Significance of the Research

1.3.1 Intellectual Merit

This research contributes to debates on the capabilities of remote-sensing technology to detect oil in the coastal environment, particularly in the areas that have already experienced oil spills. Hyperspectral image analysis potentially allows separation of oil spills from background and produces spatial maps by exploiting the spectral signatures of oil. This is a capability that other sensor types likely do not possess. This study is significant because it focuses on the detection of oil spills in a dynamic coastal environment that needs to be more clearly understood via three different

endmember-based classification algorithms. The proposed methodology is innovative because MESMA and SID, which have been shown to be effective in other remote-sensing contexts, have not previously been used for quantitative remote-sensing detection/classification of oiled vegetation. MTMF has only used on a very limited basis in this domain.

1.3.2 Broader Impacts of Research

Two broader impacts are anticipated from this research.

Benefits to society

Currently, there are thousands of offshore petroleum and gas exploration rigs operating a few miles away from the coast of Gulf of Mexico. Unexpected accidents may release crude oil over the sea surface and along coastline. Therefore, for the environmental agencies such as coastal conservation agencies, it is important to know how to manage with oil spills in a short and long term. This research provides a new methodological approach for identification and mapping oil spills in coastal environment. The detailed methodology described in this thesis will enhance the efforts of early oil slick detection and mapping during any emergency response in order to minimize the effects of oil spill to the coastal wetlands. Therefore, this study is also important in understanding the ecological and morphological impacts of oil spills on the marshlands, and along the coastline and tidal channels for the coastal wetlands

conservation agencies of Louisiana, as well as similar entities/agencies in other coastal areas.

Enhancing scientific/technological understanding

This research underlines the critical importance of remote-sensing technology and particularly emphasizes hyperspectral remote sensing in the application of oiled vegetation detection. This study will help to better establish a stronger understanding of the different factors affecting accuracies of oiled vegetation detection, which will contribute to future research by other scholars. It is expected that the methods investigated here will provide the scientific community with an improved understanding of the effectiveness of AVIRIS data in this application domain. This methodology and knowledge can be applicable to different oil- spill related studies such as management, mapping, and monitoring. In addition, the results of this research will be distributed to the various scientific communities through publication in scientific journals.

1.4 Organization of the Research

The thesis is composed of six chapters. The content of each chapter is summarized below.

Chapter I is an introduction to the subject of this research, its motivations and objectives including the significance and broader impacts of this research. Furthermore, the information about the study area of the research is provided in this chapter.

Chapter II is the literature review which provides a coherent and comprehensive summary of imaging spectrometer and different remote sensing technologies in the application of oil spill detection and mapping both in terrestrial and aquatic environments. In addition, this chapter also provides a background about the effects of oil spill on vegetation species and ecosystems.

Chapter III is the materials and methods which include detailed information about the sensor characteristics and explain how this research was conducted by describing the methods and algorithms. Besides, the datasets used for the purpose of study and methods applied in processing the data are introduced in this chapter.

Chapter IV is the results section which represents the findings of all methods presented.

Chapter V is the accuracy assessments chapter which compares the three endmember based classification techniques based on their performance in detection of oil spilled vegetation along the Gulf of Mexico, Louisiana.

Chapter VI is the discussion and conclusion in which the potential uncertainties of data analysis are discussed, recommendations for future research are made, and the summary of findings of this thesis is presented.

CHAPTER II

LITERATURE REVIEW

The review of the literature regarding oil spill monitoring and mapping via remote sensing applications consists of three major components. First the review of different remote sensing instruments and the oil spill detectability of these sensors under varying conditions. Second the review of oil spill detection studies via analysis of the AVIRIS image data. Third the review of oil spill impacts on vegetation and detection of oiled marsh vegetation via remote sensing methods.

2.1 Oil Spill Detection and Remote Sensing

Multiple instruments are capable of detecting oil spills using spaceborne and airborne platforms such as radar (synthetic aperture radar (SAR), side-looking airborne radar (SLAR)), UV, microwave radiometers, photographic cameras, video cameras, electro-optical sensors within the visible and infrared, and laser fluorosensors. As the studies of Fingas and Brown (1997) and Brekke and Solberg (2005) conclude, each instrument has strengths and deficiencies, so there is no single instrument that is best at detecting oil spills. Active sensors such as SAR have been commonly used for oil-spill detection due to their all-weather and all-day operation capabilities. From the sea surface, oil-related materials can be identified as dark spots. Therefore, dark-spot detection is a critical and fundamental step for the detection and monitoring of oil spill in

a marine environment (Shu *et al.*, 2010). Researchers investigate sources that cause different oil slicks over the sea surface. They classified oil slick signatures on SAR images of the sea surface into three types: natural slicks, look-alikes, and man-made oil spills. For example, Akar *et al.* (2011) state that look-alikes are produced by atmospheric and oceanic processes which yield as dark patches in SAR images similar to oil slicks. In addition, oil detection depends on the local weather conditions that determine its fate on the water's surface (Nirchio *et al.*, 2005). Therefore, oil slicks are visible only for a limited range of wind speeds (Brekke and Solberg, 2005). There are also other important limitations, such as wind speed, physical, geometrical and geographical parameters that affect oil detectability that must be taken into account in order to discriminate between oil spills and look-alikes. Most of the oil spill detection studies concentrate on single frequency and single polarization SAR images; however, Brekke and Solberg include that the differences in multi-frequency and multi-polarization signatures can provide more accurate and effective results for identification and discrimination algorithms of oil slicks. Therefore, PolSAR data can provide extra information contained in the measured scattering matrices, allowing separation of oil spills from the ocean background in a physical domain (Liu *et al.* 2009). They used two UAVSAR L-band polarimetric SAR images acquired during the Deepwater Horizon (DWH) oil spill accident in the Gulf of Mexico in 2010 to demonstrate the effectiveness of fully polarimetric SAR oil spill detection algorithms. Similarly, in a recent research Ramsey *et al.* (2011) examine the ability of the fully polarimetric high resolution L-band SAR sensor system to detect oil occurrences in wetlands area. Pre- and post-spill PolSAR images acquired by the

NASA's Uninhabited Aerial Vehicle Synthetic Aperture Radar (UAVSAR) were compared, and different decomposition methods were applied for rapid production of targeted oil-impact maps during emergency response. Migliaccio *et al.* (2007) applied the target decomposition theorem to identify oil spills from look-alikes in SIR-C/X SAR polarimetry data. Hu *et al.* (2003) proposed a method to detect and monitor oil spills in a turbid estuary. In another study in 2009, they demonstrated that MODIS imagery in conjunction with SAR imagery is capable to locate oil spills in the sea mainly under sun glint conditions. They tried to estimate the surface area of natural oil slicks in the NW Gulf of Mexico (GOM).Oil absorbs solar radiation and re-emits a portion of this energy as thermal energy. It is known that thermal infrared sensors observe thick oil slicks as hot; oil layers of intermediate thickness as cool; whereas thin oil is not possible to detect in this manner (Fingas and Brown, 1997).

2.2 Oil Spill Detection via Imaging Spectrometer Data

Regarding the use of hyperspectral data in this application domain, improvements in sensor technology have led to development of hyperspectral sensors, such as the Airborne Visible/Infrared Imaging Spectrometer (AVIRIS) (Green et al., 1998). A hyperspectral image consists of tens to hundreds of spectral bands and can provide a detailed spectral identification of a feature, such as differentiating between light and crude oil, and detecting small concentrations of oil (Klemas *et al.*, 2010). AVIRIS was the first airborne hyperspectral sensor to measure reflected solar radiation

from 400 nm to 2500 nm (Green *et al.*, 1998). Recent studies have indicated the potential for using remote sensing to characterize oil contamination on the ocean's surface by using hyperspectral images (Lammoglia & Souza Filho, 2011). The spectral reflectance of a given pixel is characteristic of the mixture of component materials on the ground; each component has its unique spectral signature. Therefore, hyperspectral remote sensing provides highly accurate information about materials based upon their spectral signatures (Campbell, 2007). In previous studies, hydrocarbon absorption features have been identified in the reflective region of the electromagnetic spectrum (Hirschfeld and Hed, 1981; Cloutis, 1989; Gaffey *et al.*, 1993; Clark *et al.*, 2009). A major absorption feature was delineated at 1726 nm due to combination of symmetric and asymmetric CH2 (carbon-hydrogen) and CH3 stretches. In addition, a hydrocarbon plateau in the 2300-2450 nm spectral regions was observed because of the different combinations of the C-H bonds (Cloutis, 1989; Gaffey *et al.*, 1993). In oil spill-detection analysis, AVIRIS affords the potential for detailed identification of materials and better estimates of their abundance. This can minimize false alarms of features which may be mistakenly identified as oil spill by conventional multispectral sensors. The calibration to remove the effects of atmosphere on the apparent surface reflectance is a critical pre-processing step for the detection of oil spills. Salem *et al.* (2002) conducted research on the monitoring of oil-slick movements, and the detection of spills along the shoreline. Utilizing oil spectral-feature analysis, the authors attempted to classify light oil and heavy oil. Salem *et al.* (2001) introduced a method by using spectral information provided by hyperspectral data to extract the spectral signature of oil and also to

discriminate different types of oil such as crude or light oil on the sea. In another similar study by Salem *et al.* (2004) conducted a research in order to monitor oil slicks movements, and identify spills on the shoreline. They performed the Spectral Angle Mapper (SAM) to identify oil spills and oil dispersant in water and shoreline. In another study, Clark *et al.* (2010) examined a method to derive oil thickness and the oil: water ratio from remotely-sensed NIR spectral absorption features. They applied a spectral feature identification method to data collected with the NASA AVIRIS sensor. Oil slicks with different thicknesses will lead to different spectral reflectance within the electromagnetic spectrum. The key aspect of the oil-spill detection method is a spectral feature analysis of two hydrocarbon absorption features, centered near 1.72 and 2.3 μm, which arise from the C\H bonds in oil (Cloutis, 1989). Salem and Kafatos (2001) found that a signature matching method based on airborne hyperspectral imaging is more accurate than conventional techniques, where the analysis is based on visual interpretation of oil color and its appearance in the satellite image. Sidike *et al.* (2012) applied spectral unmixing and partial spectral unmixing methods for oil spill detection in the ocean using the AVIRIS images. The results show that the partial unmixing technique, called Constrained Energy Minimization (CEM), provides the best result for oil spill detection. In recent research, Kokaly *et al.* (2013) have applied a spectroscopic analysis to AVIRIS data collected from low and medium altitudes during and after the Deepwater Horizon oil spill to detect oiled areas with physically-damaged canopies in the marshes of Barataria Bay. They used the hydrocarbon absorption features centered

near 1.72 and 2.3 μm, which arise from the C\H bonds in oil (Cloutis, 1989) in order to detect oiled vegetation.

2.3 Effects of Oil on Vegetation

The proposed study focuses on hyperspectral remote-sensing detection of oiled marsh vegetation. Oil spills can occur in both aquatic and terrestrial ecosystems; therefore, in order to understand the environmental impacts of oil spills on the dynamic ecosystem, the hydrocarbon contamination needs to be investigated on a large geographic scale, including vegetation, sediment etc., in addition to marine environments (Sammarco *et al.*, 2013). Marshes, which constitute a major component of river, estuarine and coastal ecosystems, are extremely sensitive to oil pollution (Vega *et al.*, 2009). Several studies have investigated petroleum hydrocarbon impacts on coastal ecosystems. Pezeshki *et al.* (2000) summarized the effects of petroleum hydrocarbons on marsh in two categories; the first one is chemical impacts of oil on vegetation, which vary greatly due to oil type and amount. The second effect is the physical impacts of oil on vegetation by coating of the plant foliage and soil surfaces. Oil reduces the transpiration rate by blocking stomata and intercellular spaces, and it causes reduction of photosynthesis. Therefore, critical changes are expected on the reflectance properties of vegetation species due to physical and chemical effects of oil. Based on this knowledge, this research aims to discriminate oiled vegetation from non-oiled vegetation. In this context, remote sensing can provide valuable information. For instance, Gilfillan *et al.*

(1995) performed an image analysis of historical aerial photographs to examine the effects of the Amoco Cadiz oil spill on marsh ecology, and they conclude that there were dramatic reductions in total vegetated area in the marshes due to the oil spill. Li *et al.* (2005) conducted a study to evaluate the potential of hyperspectral AVIRIS data to identify vegetation stress caused by petroleum contamination. They performed various analyses, including those based on vegetation indices (VI), "red-edge" detection, band absorption analysis, spectral mixture analysis, wavelet transform, and artificial neural networks. They concluded that the variation in vegetation spectra demonstrates the biochemical consequences due to oil stress. In another study, Mishra *et al.* (2012) quantified the short-term oil-spill impact on coastal salt marshes over a large area by combining Landsat data with ground experiments. Lin *et al.* (1996) mentioned that the impacts of oil on vegetation may exhibit several differences due to type of species, extent of oil coverage, and the season of the spill. Thus, detection of oil-impacted vegetation with remote sensing is challenging. Ramsey *et al.* (2011) examine the ability of a fully polarimetric, high-resolution L-band SAR sensor system to detect oil occurrences in wetland areas. Pre- and post-spill PolSAR images acquired by NASA's Uninhabited Aerial Vehicle Synthetic Aperture Radar (UAVSAR) were compared, and different decomposition methods were applied for rapid map production of targeted oil-impacted areas during emergency response.

This research utilizes Multiple Endmember Spectral Mixture Analysis (MESMA), a modified version of Spectral Mixture Analysis (SMA), to detect and classify oil spills within a set of AVIRIS images acquired over the Barataria Bay,

Louisiana. Roberts *et al.* (1998) developed multiple endmember spectral mixture analysis (MESMA), which allows endmembers to vary on a per-pixel basis. This study will also assess the classification accuracies of Mixture Tuned Matched Filtering (MTMF) (Boardman, 1998) and spectral information divergence (SID) (Kullback, 1959) as baseline algorithms. Oil spills occur in both aquatic and terrestrial environments. There are various efforts to provide more accurate oil-mapping methods; however, few studies have focused on comparing the efficacies of multiple algorithms for detecting oiled vegetation. This proposed research will fill this gap by processing different airborne sensor images. This research seeks to evaluate the relative advantages and disadvantages of different available hyperspectral-mapping algorithms in this application domain.

CHAPTER III

MATERIALS AND METHODS

The data sets used in this research consist of hyperspectral images acquired using the Airborne Visible/Infrared Imaging Spectrometer (AVIRIS), the Shoreline Cleanup and Assessment Team (SCAT) oiling maps along Barataria Bay, Louisiana and NAIP orthophotographs. In addition, spectral information regarding healthy vegetation, oiled vegetation, and oiled dry marsh was utilized as ancillary data which are published in Kokaly *et al.* (2013).

3.1 Data Sets

3.1.1 Airborne Imaging Spectrometer Data

In this research, hyperspectral AVIRIS images acquired near the time of the Deepwater Horizon accident in the Gulf of Mexico were analyzed in order to detect potential oiled marsh vegetation along the Gulf of Mexico coastline in southern Louisiana, USA. Four AVIRIS images, covering the vicinity of the Barataria Bay were used for developing/testing the proposed methodology. The AVIRIS hyperspectral image is obtained using the AVIRIS scanner from the Jet Propulsion Laboratory (JPL) that was installed on the NGS aircraft. The AVIRIS is a unique optical sensor that contains 224 different detectors, with a spectral bandwidth of approximately 10 nanometers (nm) which allows covering the entire range between 380 nm and 2500 nm.

The AVIRIS is a whiskbroom scanning system, and it is flown as a research instrument on the NASA ER-2 aircraft at an altitude of approximately 20 km at about 730 km/hr, resulting in approximately 20 m pixels and a 10.5 km swath width. Since 1998, it has also been flown on a Twin Otter aircraft at low altitude—approximately 4 km above sea level at about 130 km/hr, yielding 2- to 4-m spatial resolution. The AVIRIS sensor collects data that can be used for characterization of the Earth's surface and atmosphere from geometrically coherent spectroradiometric measurements. The AVIRIS represents the current state-of-the-art airborne hyperspectral system (Porter and Enmark, 1987; Green *et al.*, 1998). Hyperspectral data provide more information compared to multispectral data since it contains both spatial and spectral information from materials which are typically collected as a hyperspectral data cube.

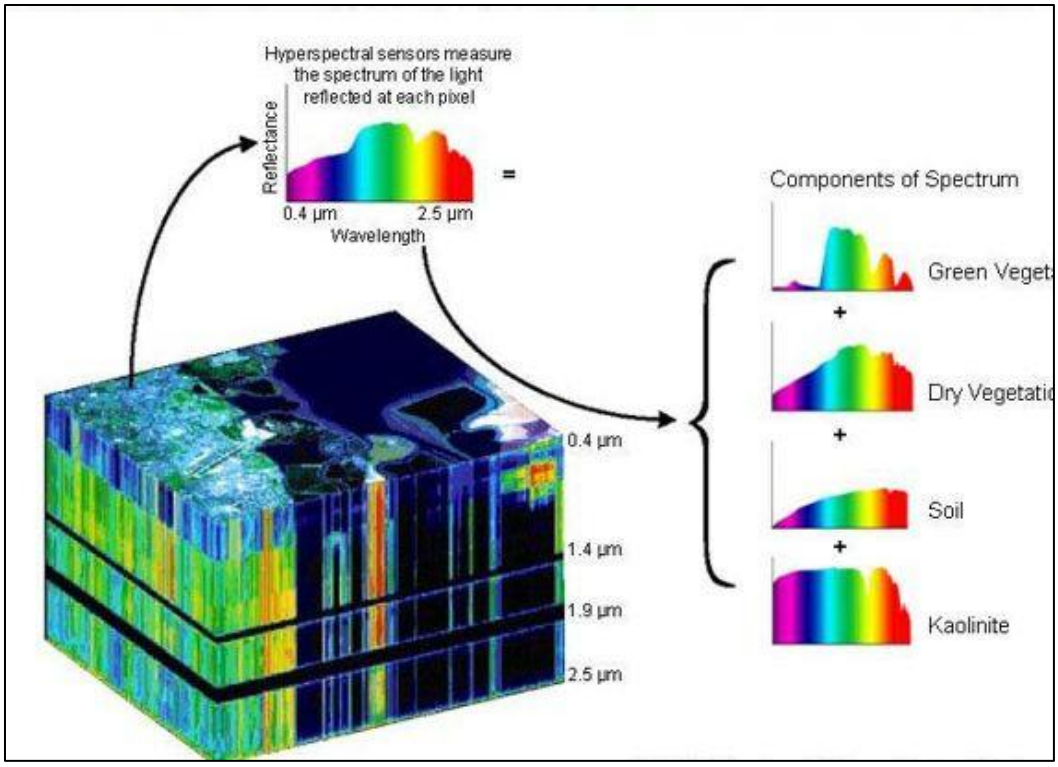

Figure 3 Concept of Hyperspectral Imagery (Image Source: NEMO Project Office, United States Navy, 2004).

The spectral cube is a three-dimensional array containing spatial resolution on the x- and y-axis, the number of contiguous spectral bands of the image on the z-axis. The dimensional thickness of z indicates the number of bands. Therefore, the combination of all wavelengths in a given spatial area provides complete spectral signatures of endmembers present in the scene (Figure 3). National Aeronautics and Space Administration (NASA) organized flights of advanced remote-sensing instruments to support the national oil-spill response during the Deepwater Horizon incident. As part of that response, data were collected using AVIRIS between 6 May and 4 October, 2010 at the request of the National Oceanic and Atmospheric Administration.

AVIRIS extensively mapped the region affected by the spill during 456 flights in order to detect and quantify thick oil emulsions on the surface. Figure 4 shows the 456 AVIRIS scenes that were collected as part of the scientific response to the Deepwater Horizon oil spill in the Gulf of Mexico. In this research four spatially-contiguous AVIRIS images are selected for oiled vegetation-detection analysis among those 456 AVIRIS scenes; these scenes are: f100914t01p00r02, f100914t01p00r03, f100914t01p00r04, and f100914t01p00r05 (Figure 5). All AVIRIS images were downloaded from the NASA JPL Gulf Oil Spill Archive (http://aviris.jpl.nasa.gov/html/gulfoilspill.html).

Figure 4 AVIRIS flights over the Gulf of Mexico (Image Source: NASA JPL Gulf Oil Spill Response).

The first AVIRIS image consists of 1,068 samples and 10,635 lines, with 224 bands and a ground pixel size of 3.5 m × 3.5 m, which may be appropriate for identification of oil spills along the coastline and adjacent terrestrial environment. The wavelength range of the sensor is from 365.92 nm to 2496.23 nm, and the spectral interval is approximately 10 nm. The second AVIRIS image consists of 1,052 samples and 10,780 lines, with 224 bands and a ground pixel size of 3.5 m × 3.5 m. The third AVIRIS image consists of 1,189 samples and 11,949 lines, with 224 bands and a ground pixel size of 3.4 m × 3.4 m. The fourth AVIRIS image consists of 1,155 samples and 11,896 lines of 224 bands, with a ground pixel size of 3.5 m × 3.5 m. The data were collected on 14 September 2010 at altitudes of 4.15, 4.21, 4.24, 4.21 km, respectively. Each AVIRIS scene was first radiometrically corrected at the JPL in order to remove fundamental geometric errors associated with the motion of the vehicle during collection. Atmospheric correction must also be applied to remove further errors due to atmospheric effects such as absorption. Spectral analysis and classification techniques were performed by using the photogrammetric and remote-sensing software, the ENvironment for Visualizing Images™ (ENVI™) version 4.8.

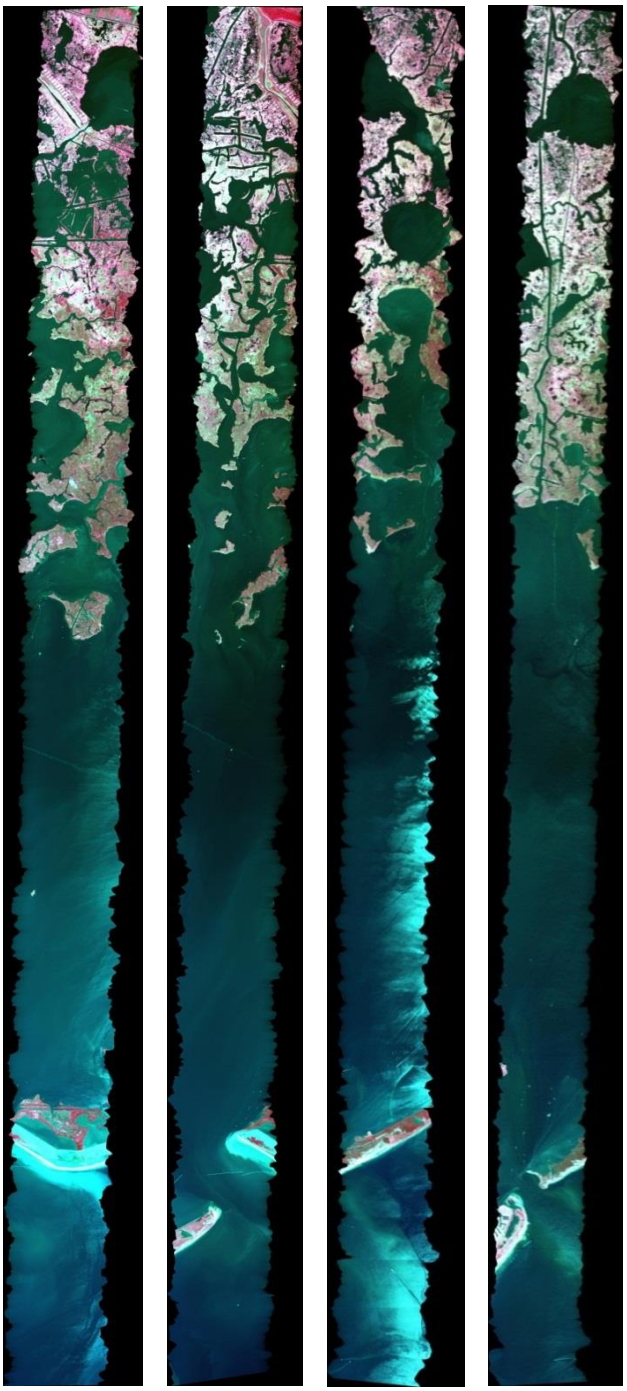

(a) (b) (c) (d)

Figure 5 The full AVIRIS color-composite images, displayed with bands 44, 31, and 21 as R, G, B, acquired on September 14, 2010 over the Barataria Bay, LA, USA. (a) is the first AVIRIS image with scene ID f100914t01p00r02. (b), (c) and (d) are the second,third and fourth AVIRIS image with scene IDs f100914t01p00r03, f100914t01p00r04 and f100914t01p00r05, respectively.

3.1.2 SCAT Data

The Shoreline Cleanup and Assessment Team (SCAT) survey consists of a team walking the shoreline or transiting close to shore by boat. The major purpose of SCAT team is to document several critical terms of oiling such as oil character, thickness, percent distribution, width and length of the oiled bands, tidal zone where the oil bands were observed, the average and maximum size of oil deposits (NOAA, 2011). The SCAT process was originated during the response to the 1989 Exxon Valdez oil spill (Owens, 1990). During the Deepwater Horizon response, the Unified Command managing the emergency response (lead by the Federal On-Scene Coordinator [U.S. Coast Guard] in consultation with the State On-Scene Coordinators from each State, and BP) established a Shoreline Cleanup Assessment Technique (SCAT) Program on 28 April 2010 (Michel *et al.*, 2013). The presence and/or absence of oil along the coastline of the Barataria Bay were reported on a nearly daily basis by SCAT (Boopathy, 2010). 18 SCAT teams, consisting of Federal, State, local, and BP representatives, conducted field surveys to document the location, degree, and character of shoreline oiling. SCAT data on oiling characteristics were used routinely to generate maps and tabular data on degree of oiling by habitat over time. Oiling degree categories (heavy, moderate, light, very light, trace) were defined based on the width of oiling bands on the shoreline (as measured perpendicular to the shoreline), the percent cover of oil within the band, and oil thickness using a two-step process. These data were the basis for verification of the findings from this research. Nearly all oil remnants resulting from the Deepwater

Horizon accident have already been cleaned due to extensive cleanup effort. Therefore this situation made it impossible for this research to conduct fieldwork to the study area covering Bay Jimmy, Bay Chene Fleur, and Wilkinson Bay in southern Louisiana. The data from September 17, 2010 was requested from the National Oceanic and Atmospheric Administration (NOAA) (Figure 6). This data includes detailed oil spill map along the coastline of the Gulf of Mexico and summarizes the data collected in the field. It provides accurate information for accuracy assessments, since the *in situ* data acquisition is slightly after the AVIRIS image acquisition time which is September, 14 2010.

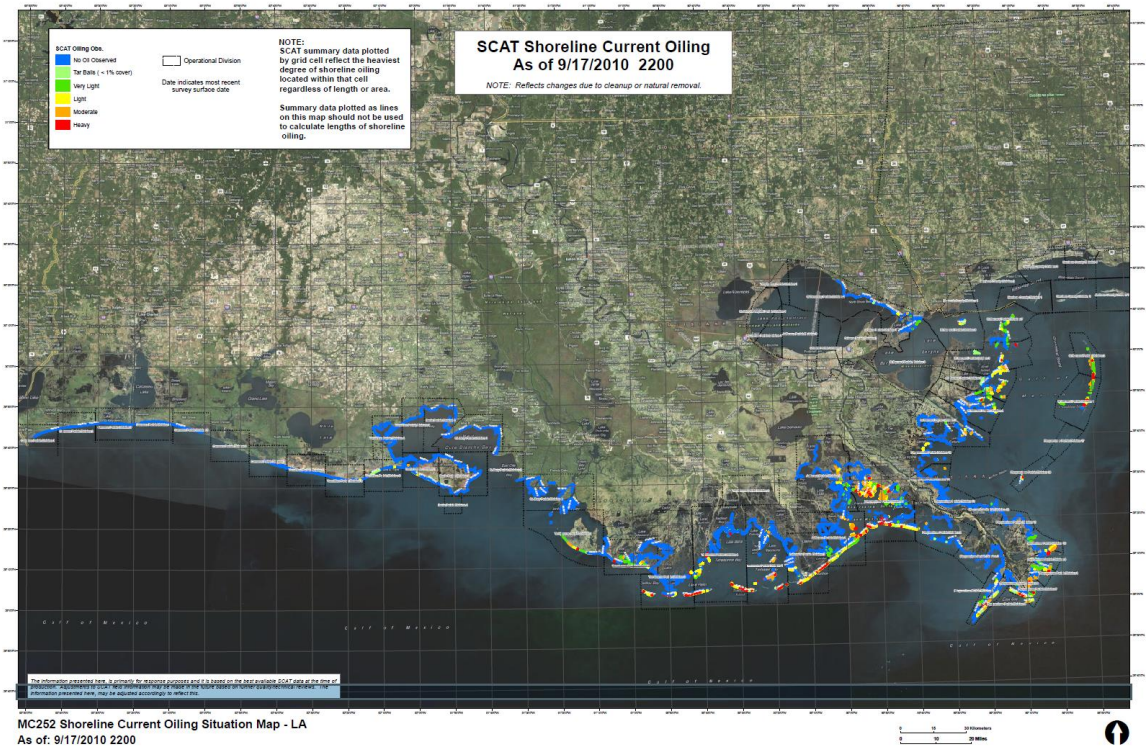

Figure 6 NOAA SCAT Map showing oiling degree categories along the Gulf of Mexico coastline as of September, 17 2010. The red box indicates the study site of this thesis. (URL: [gomex.erma.noaa.gov/erma.html])

3.1.3 Aerial Imagery

Image data from the National Agriculture Imagery Program (NAIP) were used as reference data for accuracy assessments. NAIP images are aerial photographs acquired during the agricultural growing season across the United States. Such images have a 1-m spatial resolution and are collected in natural color and/or color-infrared. All images are inspected for horizontal accuracy (required to be within 6 m of identifiable ground control points) and tonal quality. NAIP end products are digital orthorectified photographs that are available to the public within one year of acquisition. The aerial photographs were downloaded from the Unites States Department of Agriculture (USDA) website (http://datagateway.nrcs.usda.gov/GDGOrder.aspx). The NAIP images used in this research were acquired on 5 May and 10 November 2010, which is before and slightly after the acquisition of the AVIRIS images, respectively.

3.2 Image Preprocessing

There are many factors which affect the quality of the hyperspectral image data, ranging from the external factors to the internal factors such as sensor noise and sensor characteristics. Before continuing with further image-processing steps, AVIRIS spectral overlap channels (bands 33, 34, 97, 98, 160, 161 and 162) were discarded, leaving 217 bands. The resulting image was then used as input to atmospheric correction algorithm

and the remaining channels were examined in terms of noise after atmospheric correction.

After the atmospheric correction, the bands with numbers 1-4, 107-116, 153-170, 223 and 224 were selected as visually noisy and removed, resulting in a 186-band hyperspectral image. A total of 186 bands out of 224 bands were thus subjected to subsequent analyses, after eliminating the first few bands at wavelengths shorter than 400 nm, the bands dominated by noise, as well as the spectral-overlap bands. All other image-processing techniques and mapping methods were applied to the noise-reduced and spectral overlap-discarded data. Due to the high number of channels, the size of the hyperspectral data set is large, and the processing usually requires long execution times. Therefore, in addition to eliminating some bands, the four AVIRIS images were spatially-subset in order to increase efficiency in terms of processing time for all image-processing operations. The portions of the images that contain mostly water were excluded, whereas those portions containing mostly land were retained for further analyses. The resulting spatial subsets are given in Figure 7. Spatially-subsetting the larger images enable the analysis to focus on the regions of the scenes that are of primary interest in this study.

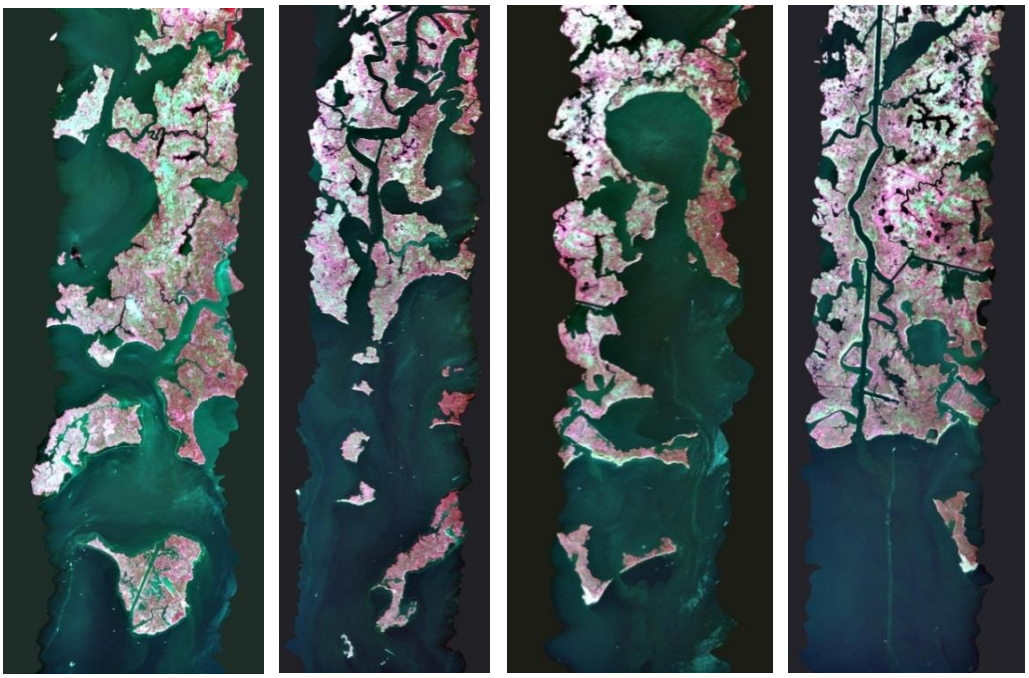

(a) (b) (c) (d)

Figure 7 Retained spatial subsets of the full AVIRIS images, displayed with bands 44, 31, and 21 as R,G,B, where portions of the full images that contain mostly water were excluded.a) is the first AVIRIS image with scene ID f100914t01p00r02. (b), (c) and (d) are the second,third and fourth AVIRIS image with scene IDs f100914t01p00r03, f100914t01p00r04 and f100914t01p00r05, respectively**.**

3.2.1 Atmospheric Correction

In order to achieve significant spectral signatures of the ground features, several preprocessing steps were applied to the AVIRIS hyperspectral images such as atmospheric correction, noise reduction. Each AVIRIS scene was first geometrically corrected at the Jet Propulsion Laboratory. It was then atmospherically corrected to surface reflectance using ENVI™ version 4.8. Atmospheric correction of satellite images is a critical image-preprocessing step, where the effects of the atmosphere are removed or markedly minimized. A variety of atmospheric-correction algorithms are available. In

this research, radiometric correction using the Fast Line-of-sight Atmospheric Analysis of Spectral Hypercubes (FLAASH) algorithm was performed on the data. FLAASH is an ENVI™ module for retrieving spectral surface reflectance from hyperspectral radiance images. It is an efficient tool for pre-processing developed by Spectral Sciences, Inc., under the sponsorship of the U.S. Air Force Research Laboratory in order to improve the analyses of visible to shortwave infrared hyperspectral and multispectral imaging sensors (Matthew *et al.* 2000). The main objectives of FLAASH are to remove atmospheric effects caused by scattering and absorption and to convert radiance images to surface reflectance images.

FLAASH uses the MODTRAN4 radiation transfer code in conjunction with standard MODTRAN model atmospheres and aerosol types. A correction for the "adjacency effect" pixel mixing due to surface-reflected radiance scattering and a function to compute the average scene visibility are also included with the utilities in FLAASH. It convert radiance image to surface reflectance and also provides cloud classification, and water vapor images as output images. In order to correct the AVIRIS image with FLAASH the specific image parameters are necessary which are sensor type, pixel size, ground elevation, scene center latitude/longitude, sensor altitude, visibility, flight date and flight time, atmospheric model, aerosol model, water vapor retrieval, spectral polishing, wavelength calibration. The input parameters necessary for FLAASH atmospheric correction are described below for the first AVIRIS scene with the ID f100914t01p00r02. Sensor type, for the present study is selected as AVIRIS. The image average time of collection (day/month/year) was available in the metadata file. The data

were collected at 15:46 GMT on 14 September 2010. The latitude of calibrated AVIRIS image center is at 29°25'14.88"N and the longitude is 89°52'59.99"W. The sensor altitude was 4.1453 km, the average ground elevation was 0.3 m as derived from a USGS DEM, and the pixel size was 3.5 m. A visibility of 27.94 km was found to produce the best fit for the path radiance. Selection of FLAASH atmospheric model is based on latitudinal/seasonal dependence of surface temperature of the study area. Based on the location of study site for a September scene Mid-Latitude Summer (MLS) was selected along with the maritime aerosol model (Table 1). The use of FLAASH requires the sensor to incorporate the at least one of the following spectral ranges for atmospheric correction: 1050-1210 nm, 870-1020 nm and 770-870 nm with a spectral resolution of 15 nm or better. Since the appropriate bands are available, the water retrieval option was set to "Yes". FLAASH includes a method for retrieving the water amount for each pixel, in this study the 1135 nm was selected for the water absorption feature. The entire spectral range of the dataset must be known, as well as the Full Width Half Minimum (FWHM) for each band and any gain and offset values used to convert the digital number (DN) values to radiance, preferably available in ASCII *.txt files. Spectral polishing provides artifact suppression. The absorption feature of 1135 nm was selected as recommended in Exelis FLAASH User's Guide (2009).

Table 1 Selection of MODTRAN model atmospheres based on latitudinal/seasonal dependence of surface temperature (Source: Exelis FLAASH User's Guide, 2009). The intersection of September and Latitude (-20) **°N** represents the aerosol model used in this research.

Latitude (°N)	**January**	**March**	**May**	**July**	**September**	**November**
80	SAW	SAW	SAW	MLW	MLW	SAW
70	SAW	SAW	SAW	MLW	MLW	SAW
60	MLW	MLW	MLW	SAS	SAS	MLW
50	MLW	MLW	MLW	SAS	SAS	SAS
40	SAS	SAS	SAS	MLS	MLS	SAS
30	MLS	MLS	MLS	T	T	MLS
20	T	T	T	T	T	T
10	T	T	T	T	T	T
0	T	T	T	T	T	T
-10	T	T	T	T	T	T
-20	T	T	T	MLS	**MLS**	T
-30	MLS	MLS	MLS	MLS	MLS	MLS
-40	SAS	SAS	SAS	SAS	SAS	SAS
-50	SAS	SAS	SAS	MLW	MLW	SAS
-60	MLW	MLW	MLW	MLW	MLW	MLW
-70	MLW	MLW	MLW	MLW	MLW	MLW
-80	MLW	MLW	MLW	MLW	MLW	MLW

Outputs from the FLAASH correction include a surface-reflectance image, a cloud classification map, and a water vapor map. The FLAASH surface-reflectance images were subset from 224 bands to 186 bands, primarily dropping bands that have strong atmospheric water vapor absorption in the SWIR. The input parameters of the rest AVIRIS scenes (f100914t01p00r03, f100914t01p00r04, f100914t01p00r05) are provided in Table 2.

Table 2 Partial FLAASH input parameters for all AVIRIS images

Partial FLAASH Input Parameters				
Scene IDs	Altitude (km)	Flight Date	Acquisition Time (GMT)	Center Coordinates
f100914t01p00r02	4.1453	9/14/2010	15:46	29°25'14.88"N 89°52'59.99"W
f100914t01p00r03	4.2062	9/14/2010	16:04	29°25'24.17"N 89°54'20.96"W
f100914t01p00r04	4.2367	9/14/2010	16:23	29°24'10.46"N 89°55'31.26"W
f100914t01p00r05	4.2062	9/14/2010	16:43	29°24'22.10"N 89°56'42.56"W

3.2.2 Creating Water and Boat Mask

AVIRIS hyperspectral image processing includes the creation of mask of pixels that were of no interest. Thus, the first step of the image processing in this research was the elimination of any non-interest materials such as water and boats within the region of interest prior to further analysis. The water and boat features were identified to mask out in order to create a land-only image. The method used to separate the water and land from a remotely sensed image is based on the spectral difference between water and land. Masking of water was carried out by using AVIRIS band 153. After creating water mask, polygons were produced by drawing region of interests (ROIs) covering the surface features including boats and the waves induced by boats in order to analyze only land (Figure 8). After building the water and boat masks for all images, which are given

in Figure 9, they were applied to the AVIRIS scenes to mask classes that are not desired. Eliminating these areas allowed the analysis to focus on oil-spill areas along the coastline and adjacent backshore.

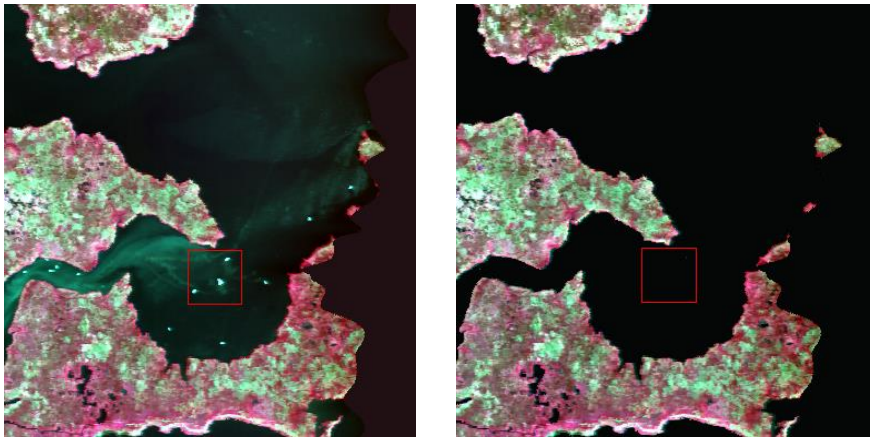

(a) (b)

Figure 8 Masking of non-interest features over the scene, (a) is the original AVIRIS image including boats and water, (b) is the masked, only land image in which all non-interest materials were eliminated.

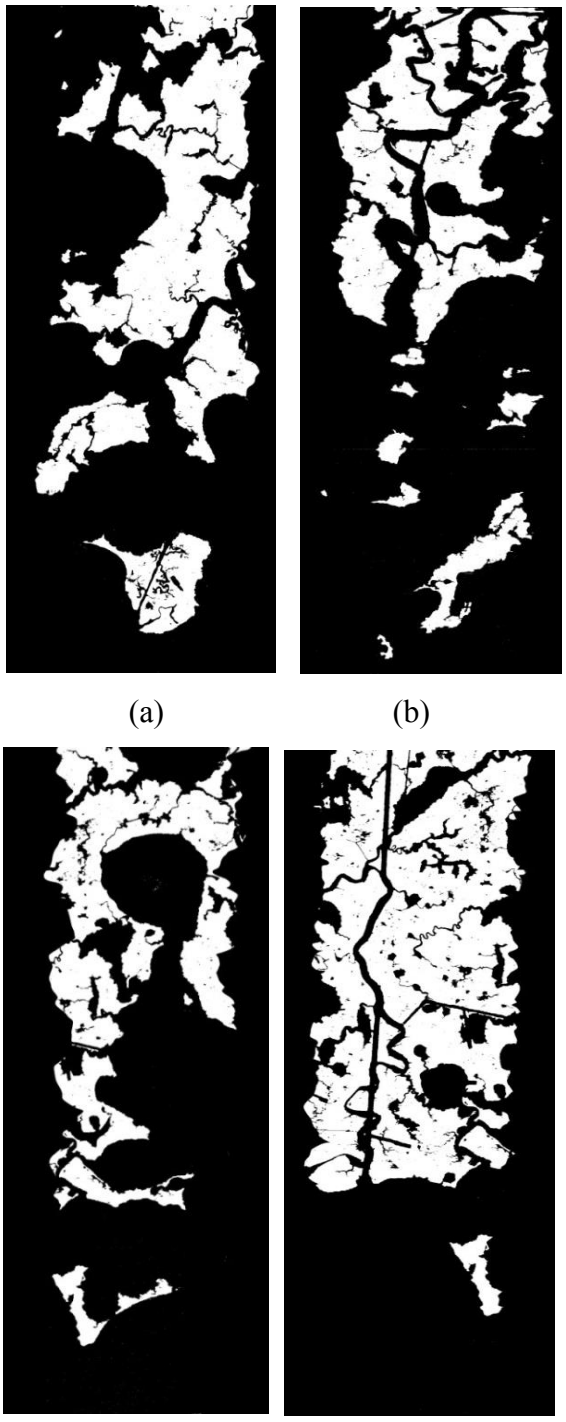

(a) (b)

(c) (d)

Figure 9 Combined water and boat masks applied to the AVIRIS scenes to create only land image, (a) is the water and boat mask for the first image and (b),(c) and (d) for the second, third and fourth AVIRIS images, respectively.

3.3 Minimum Noise Fraction Transformation (MNF)

Once all appropriate water and boat masks were created for four only land AVIRIS images separately, the next step is the reduction of the spectral dimensionality of the imagery. There are 224 bands in each AVIRIS data. However many of these bands contain redundant information. Minimum Noise Fraction Transform (MNF) is designed to eliminate redundancy and segregate any noise in the image (Boardman and Kruse, 1994). The MNF transformation was first developed as an alternative to the principal components analysis (PCA). It has all the properties of the PCA, including the primary characteristic of optimally concentrating the information content of the data in as small a number of components as possible (Lee *et al.*, 1990). The MNF transform implemented in ENVI™ is modified from Green *et al.* (1988) and defined as two-step cascaded PCA. The first rotation is based on an estimated noise covariance matrix which decorrelates and rescales the data noise. The second rotation is a standard PCA of the noise-whitened data creates a set of components that contain weighted information about the variance across all bands in the raw dataset. The MNF transformation is chosen for this study because it is an efficient technique for reducing a large multiband data set into small number components that contain the majority of information. In addition MNF orders components in terms of image quality. The contribution of each component to the overall information in a multivariate data set is measured by an eigenvalue. The resulting MNF images with the highest eigenvalues indicate that they contain more information for further processing steps. According to Smith *et al.*, (1985) and Boardman (1993)

spectrally pure pixels (i.e. endmembers) can be found at the vertices of the polygon that bounds the data space of the principal components; whereas the mixed pixels within the regions defined by these endmembers. The number of endmembers in the image is generally one more that the number of principal components, excluding noise and including shade (Adams *et al.*, 1993). The number of bands for output can be selected optionally by examining the eigenimages in terms of spatial coherency and eigenvalues. The bands containing only noise are not used in subsequent processing.

3.4 Pixel Purity Index (PPI) and *N*-Dimensional Visualizer

After selecting the number of MNF bands, the next step is to perform the pixel purity index (PPI), developed by Boardman *et al.* (1995) in order to identify pure pixels. Finding pure signatures in hyperspectral imagery is a crucial task in hyperspectral image processing and there is several endmember extraction algorithms (EEAs) developed for this purpose. One of the most popular EEAs has been the pixel purity index (PPI) in hyperspectral image analysis for endmember extraction (Chein *et al.*, 2006) and it is available in ENVI™ software. It is an iterative algorithm, where an iterative rule is developed to improve each of the iterations until it reaches a final set of endmembers. The PPI is defined as finding the most "spectrally pure," or extreme, pixels in multispectral and hyperspectral images (Boardman *et al.*, 1995). The output image of the PPI provides a brightness map of how often a pixel was defined to be an extreme pixel.

The results of the PPI can be used as input for the *n*-Dimensional Visualizer tool in ENVI™.

There are two alternatives to identify endmember spectra (Settle & Campbell, 1998). The first one is reference endmember which can be derived from the field, and the second option is image endmember which utilizes spectra derived from the image. According to Drake *et al.* (1999), image endmembers presents two advantages, they are easily obtained and they have the same scale of measurement as the data. Since reference spectra are not available, image derived endmembers were collected in this study.

After performing the pixel purity index, the next step is to visualize those pixels in *n*-D Visualizer in order to estimate the number of spectral endmembers and their pure spectral signatures. The *n*-D Visualizer was developed as an aid for identifying and distinguishing image pixels which correspond to mixing endmembers. ENVI's *n*-Dimensional Visualizer provides an interactive tool for estimating the number of spectral endmembers and their pure spectral signatures. Smith *et al.* (1985) and Boardman (1993) state that spectrally pure pixels (endmembers) are found at the vertices of the polygon that bounds the data space; whereas the mixed pixels lie in the central region. Since the number of endmembers in an image is usually taken as one more that the number of principal components, it is expected that if n number MNF bands is selected for further analysis, n+1 endmember will be extracted during the *n*-D Visualizer application.

3.5 Classification Algorithms

Three different image classification methods were applied to AVIRIS images in order to map oiled vegetation along, including Spectral Information Divergence, Mixture Tuned Matched Filtering and Multiple Endmember Spectral Mixture Analysis.

3.5.1 Spectral Information Divergence (SID)

Spectral Information Divergence is a supervised classification algorithm used for the detection of an oil spill along the coastline of Gulf of Mexico and adjacent coastal environment by using hyperspectral data set. The supervised classification is the essential tool used for extracting quantitative information from remotely sensed image data (Richards, 1993). SID is a spectral classification method that uses a divergence measure to match pixels to reference spectra. The smaller the divergence, the more likely the pixels are similar. Pixels with a measurement greater than the specified maximum divergence threshold are not classified. Endmember spectra used by SID can come from ASCII files or spectral libraries, or can be extracted directly from an image as an ROI average. Chang (2000) demonstrated that SID can characterize spectral variability more effectively than the common used SAM. In addition Van der Meer (2006) also reported that SID outperforms the classical spectral matching techniques such as SAM. SID considers each pixel as a random variable and uses its spectral histogram to define a probability distribution. The spectral similarity between two pixels is then measured by

the discrepancy of probabilistic behaviors between their spectra. In order to determine which pixels are included in a specific class, SID uses a threshold value. In this research, threshold values for SID classification algorithm were tested between 0.04 and 0.08, with an increment value of 0.01.

3.5.2 Mixture Tuned Matched Filtering (MTMF)

The Mixture Tuned Matched Filtering (MTMF) algorithm builds upon the strengths of both matched filtering and spectral unmixing while avoiding the disadvantages of both (Boardman, 1998). MTMF is defined as a special type of spectral mixture analysis which is based on well-known signal processing methodologies (Harsanyi & Chang, 1994). MTMF does not require a priori knowledge of the background material spectral signatures. MTMF results using endmembers from *n*-D visualization produces two set of rule images, the first one is the MTMF score image and the second is an infeasibility image. The MTMF score demonstrates the probability that the pixel contains the material that is being mapped and the infeasibility score shows the probability that the material in incorrectly mapped or are false positives. The MTMF uses two thresholds; one for the output of the matched filter (MF) and one for the infeasibility index. In this research, the tested threshold range for MF was between 0.3 and 0.7, with an increment value of 0.1. For the infeasibility index, the tested threshold range was between 3 and 8, with an increment value of 1.

3.5.3 Multiple Endmember Spectral Mixture Analysis (MESMA)

Multiple endmember spectral analysis (MESMA) is an extension of spectral mixture analysis (SMA) which addresses spectral and spatial variability within material classes by allowing the number and type of endmembers to vary on a per pixel basis (Roberts *et al.*, 1998). SMA quantifies the proportions of land surface features within mixed pixels using knowledge of each feature's pure spectral response or "endmember." A major limitation of SMA is that every image pixel is unmixed using the same endmember spectra. Multiple endmember spectral mixture analysis (MESMA) addresses these problems by testing multiple combinations of endmembers and endmember spectra for each pixel in the image (Roberts *et al.*, 1998). Thus, MESMA increases the flexibility of simple SMA. By using VIPER Tools open-software (Roberts *et al.*, 2007), MESMA unmixing can be accomplished with two, three or four endmembers, which is comprised of one, two or three endmember classes, coupled with a shade endmember (Dennison *et al.*, 2003; Roberts *et al.*, 1998). MESMA allows more than one endmember in the scene per ground component, and has proven to be effective in identifying different types of materials in a variety of environments. Various studies have successfully applied MESMA in urban and vegetated environments (Liu and Yang 2013, Thorp *et al*., 2013, Franke *et al*. 2009, Quintano *et al.* 2013). However, there has been no effort to map oiled vegetation by using MESMA and compare the classification results with different endmember-based classification algorithms. In this research, MESMA is applied to airborne AVIRIS data by the use of spatial constraints which are utilized as

criteria in discriminating different types of endmembers with similar spectral signatures in order to analyze the oil spill associated with the Deepwater Horizon accident in Barataria Bay.

CHAPTER IV

RESULTS

4.1 FLAASH Atmospheric Correction

Atmospheric correction was performed using the FLAASH algorithm, which is available in the ENVI™ software. The AVIRIS water-masked land images, which were spatially- and spectrally-subset and in units of radiance, were used as input to FLAASH atmospheric correction. FLAASH is not able to process files in BIL format, so the input files were converted to BIP format. For FLAASH correct, the units of the input file must be scaled to units of μW/ (cm^2*sr*nm); thus, the scale factor for each band was entered separately, which was provided in the metadata. FLAASH requires a number of input parameters. The input parameters used in this research are given in Chapter 3. FLAASH is designed for removal/minimization of atmospheric effects, and it converts the radiance image to a surface-reflectance image. The results of FLAASH atmospheric correction include a surface reflectance image (Figure 10), a cloud classification map, and water vapor map, for each AVIRIS image processed. As noted previously, noise bands were eliminated after atmospheric correction, leaving 186 bands of the original 224 bands. The atmospherically-corrected AVIRIS images constituted the basis of further image-processing analysis.

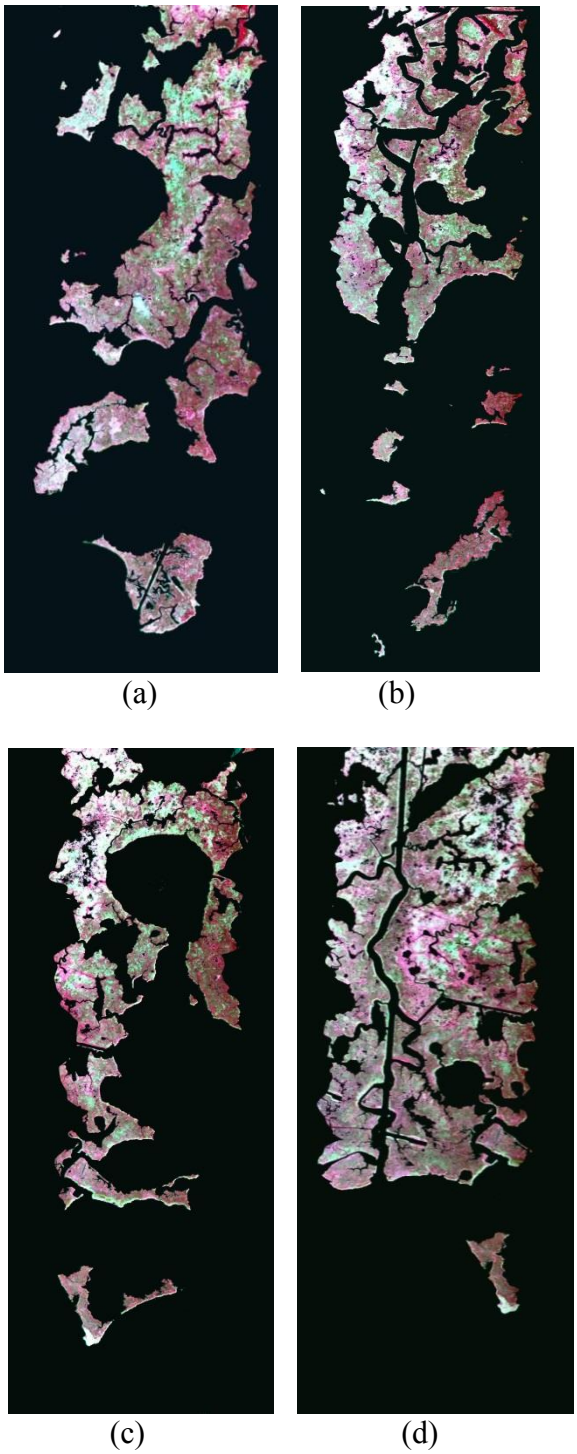

Figure 10 Surface-reflectance images of four AVIRIS subscenes over Barataria Bay, LA, USA, resulting from the FLAASH atmoshperic correction.

The spectral profile of the wetland vegetation from the raw AVIRIS data (Figure 11 (a)) and atmospherically-corrected AVIRIS image (Figure 11 (b)) were plotted in units of radiance and reflectance, respectively, in order to provide a visual comparison. The AVIRIS radiance spectrum reveals the domination of the spectrum by atmospheric effects, whereas the reflectance spectrum illustrates the spectrum after elimination of the atmospheric effects.

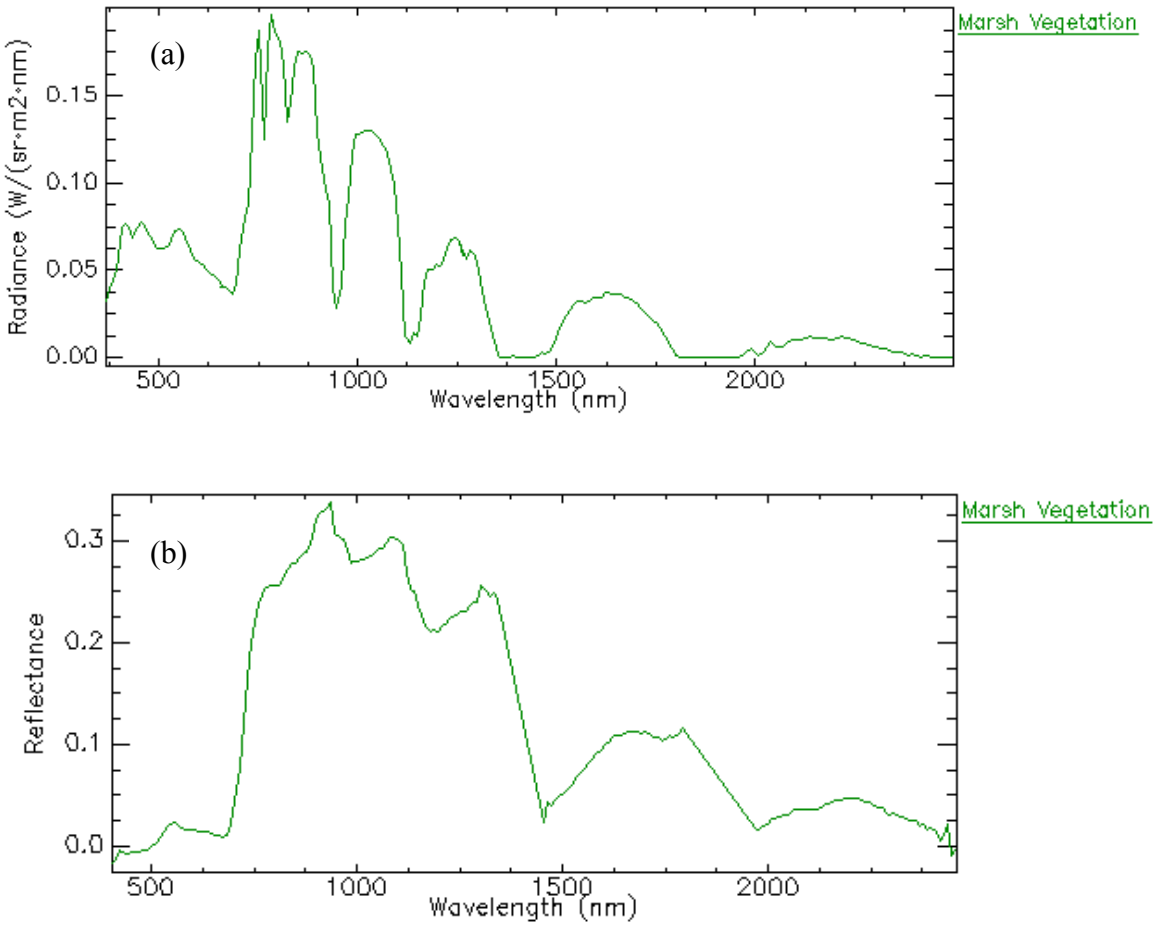

Figure 11 a) AVIRIS radiance spectrum of marsh vegetation before atmospheric correction and b) AVIRIS reflectance spectrum of the same location after FLAASH atmospheric correction.

4.2 Minimum Noise Fraction Transformation (MNF)

Before performing the MNF transform, image noise statistics were calculated. The noise statistics of the AVIRIS data were calculated from the data itself by drawing a polygon over a homogeneous portion of the image. The noise-estimation method employed is based on local pixel variance. Regarding outputs from the MNF transformation, as the band number increases, there is a decrease in spatial coherency due to noise. Typically, the first MNF band represents most of the total variance. The higher-order bands with decreasing variances are not necessary to represent the majority of the original image. Bands with large eigenvalues (greater than 1) contain data, and bands with eigenvalues near 1 contain noise. According to the MNF eigenvalue plots in Figure 12, the bands which contain the most information and the bands which contain predominantly noise can be determined. As expected, the MNF transform ordered the components in terms of image information content, as seen in Figure 13. With this knowledge, the number of MNF bands for each image to be propagated to subsequent analytical steps was determined via joint examination of the spatial coherency of the MNF images and the eigenvalues. Examination of the eigenimages and MNF scree plot revealed that the eigenvalues decrease sharply over the first 20 eigenvalues, and then flatten out. Based on this, the data were then reduced from 186 bands to the first 19 MNF bands, as these 19 eigenimages contain most of the information in the first AVIRIS image. The MNF bands dominated by noise were not used in subsequent

processing. Regarding the other three AVIRIS images, the first 18, 23, and19 MNF bands were selected for further analysis, respectively, in this research.

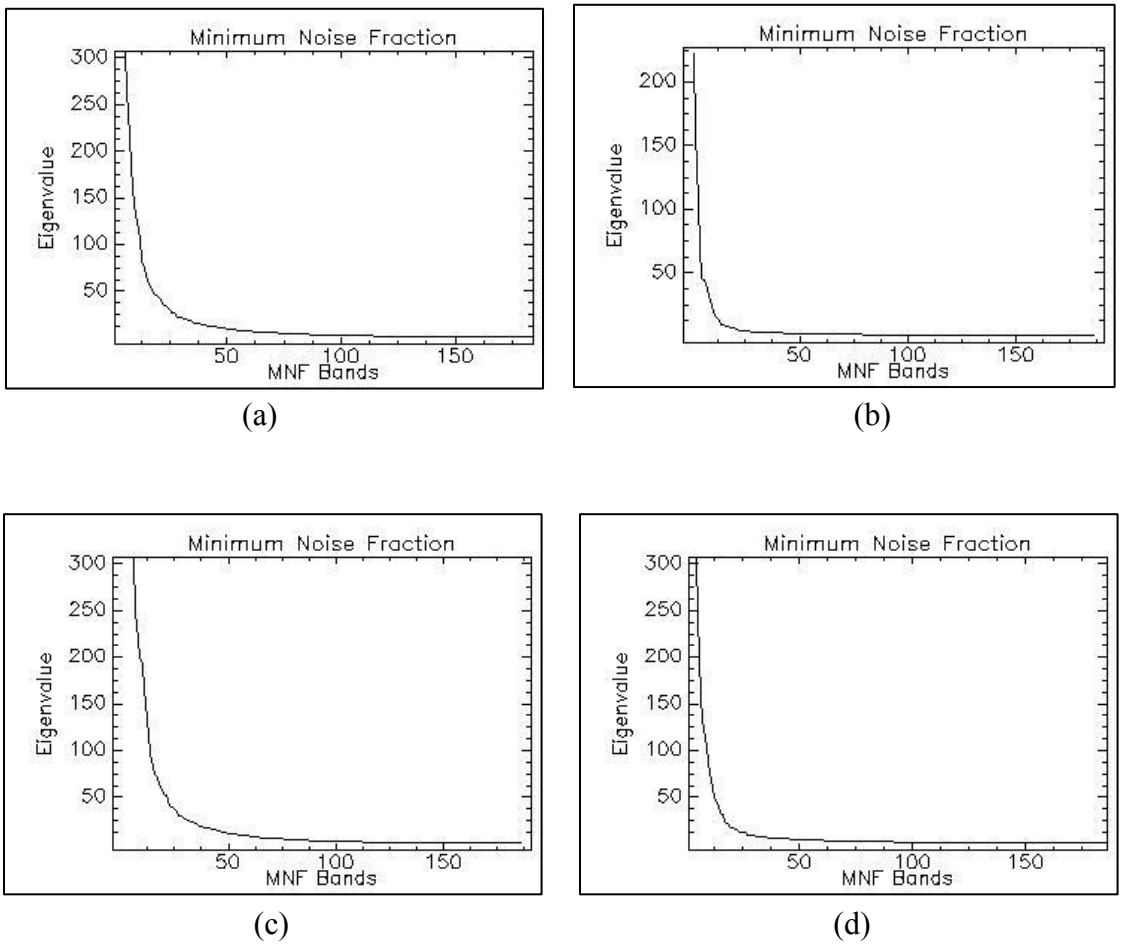

Figure 12 Eigenvalues calculated by the Minimum Noise Fraction (MNF) transform analysis. a) MNF plot for the first AVIRIS image, whereas b), c), and d) represent the MNF transformation result for the second, third, and fourth image. The first 19 eigenimages were carried forward in the analysis and contained most of the useful image information for the first image.

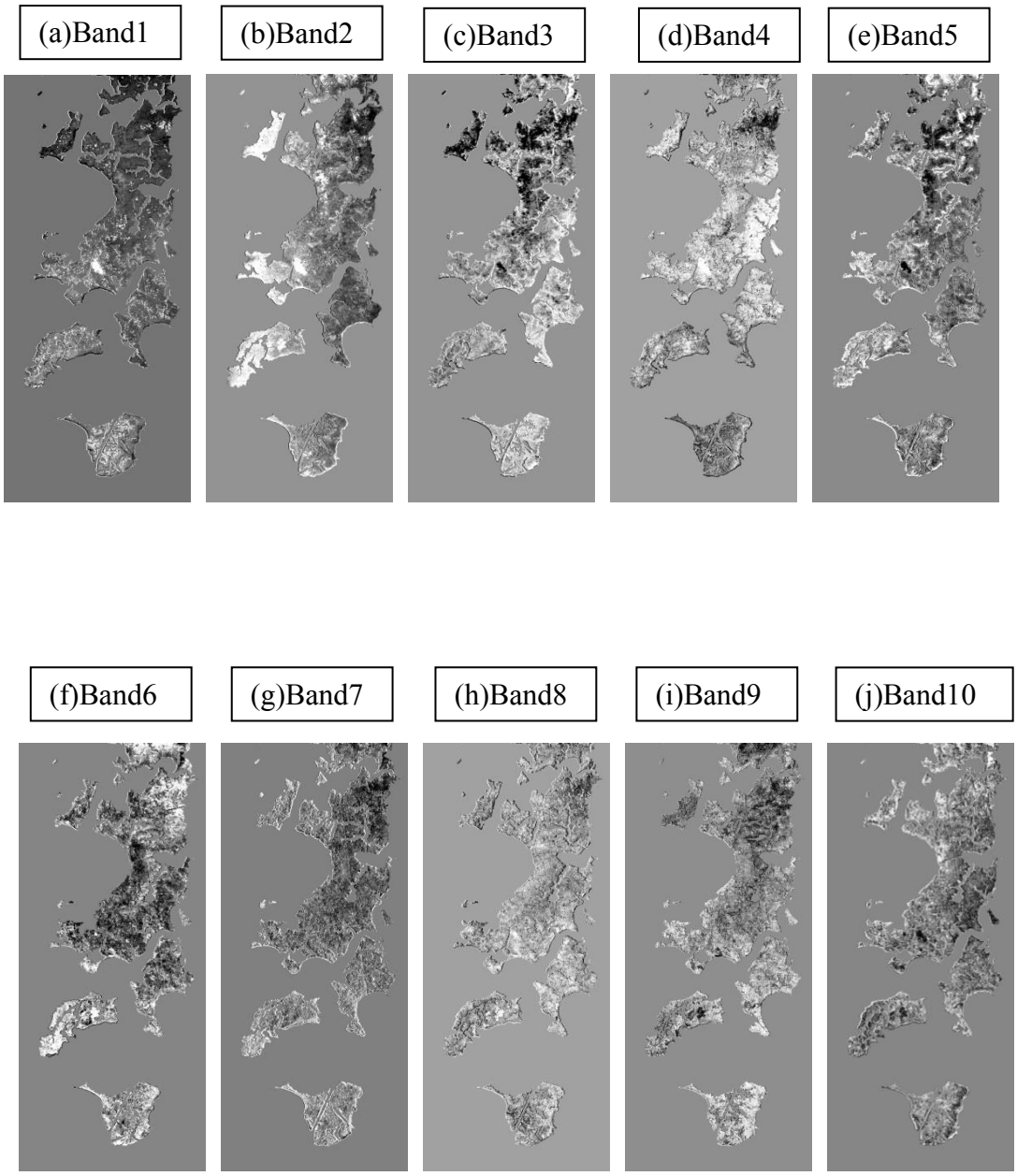

Figure 13 First 19 MNF transformed images of the hyperspectral AVIRIS image 1 with a scene ID of f100914t01p00r02.

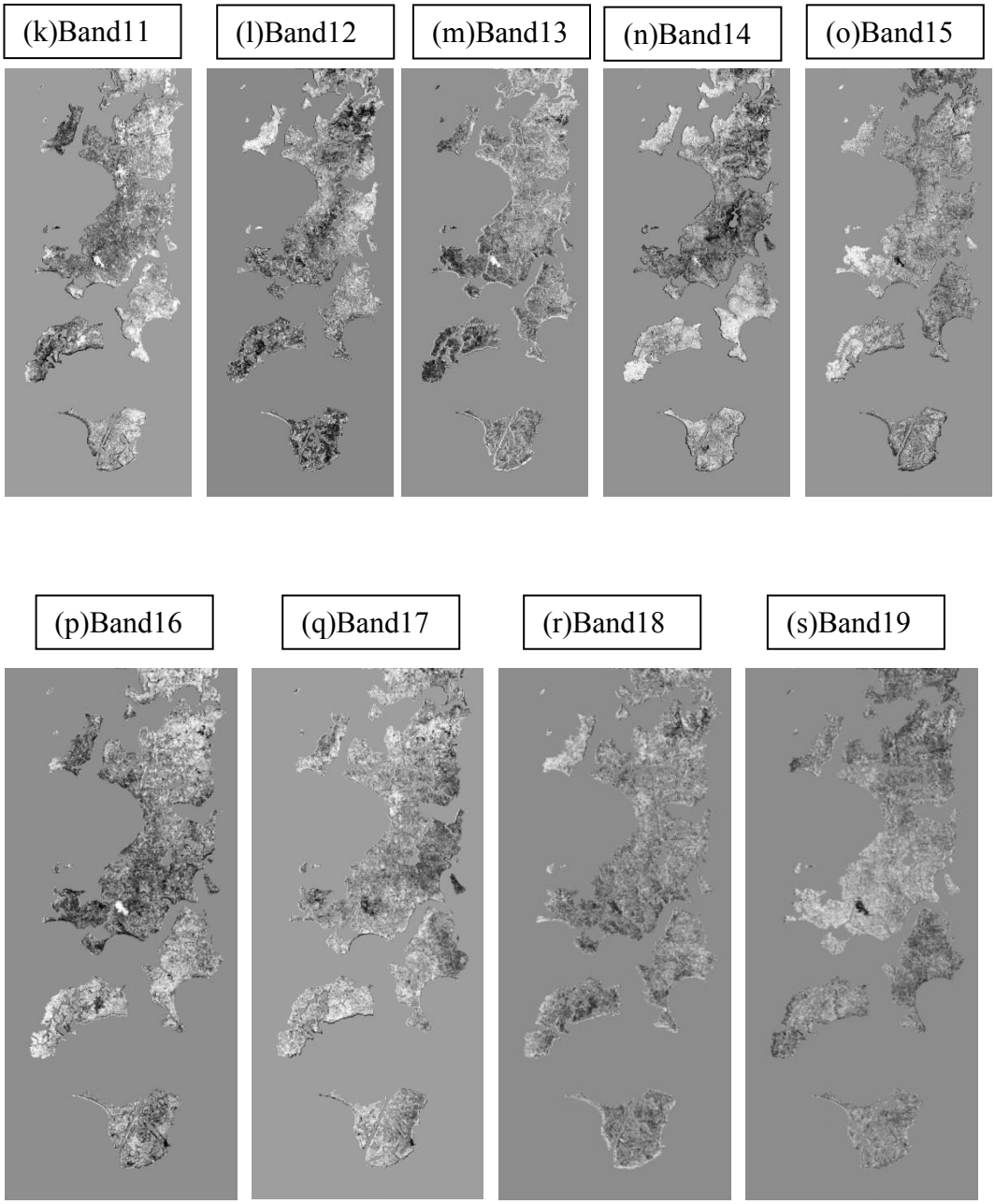

Figure 13 Continued

The MNF results for the first AVIRIS hyperspectral image are provided in Figure 13 (a)-(s), which demonstrate that higher-numbered bands contain more noise and significantly reduced image features, whereas the lower-numbered bands offer substantially higher information content. Lower-numbered bands also correspond to higher eigenvalues.

4.3 Pixel Purity Index (PPI) and *N*-Dimensional Visualizer

The Pixel Purity Index (PPI) algorithm was performed using ENVI™ image-processing software on AVIRIS images to find the most spectrally-pure pixels in the AVIRIS data. For each AVIRIS image, the PPI algorithm was applied to the MNF bands selected for further analysis, as designated in the previous section. Since it is an iterative algorithm, the user inputs appropriate parameter values, such as number of iterations, the threshold value, etc. in order to extract a significant number of potential endmember pixels (endmember candidates). In this research, several PPI iteration values were tested, starting from 10,000 and ranging to 50,000 iterations. Interactively adjusting the number of PPI iterations and the PPI threshold produced different PPI results. In general, high PPI thresholds result in more pixels in PPI resultant images, including more impure pixels marked as extreme. In contrast, a very low PPI threshold may not select many mixed pixels, but also may not select all of the purest pixels in a given image. After completing the first iteration, a few pixels in the output image have values of one, and all the rest of the pixels have values of zero. After 20,000 iterations, a few pixels may have

values between 1 and 200, but most pixels still have values of zero. Once 30,000 iterations are completed, pixels with the highest PPI values are found, and such pixels are likely closest to being corners of the data cloud representing the spectrally-purest pixels in the image. Higher iteration values have the ability to find poorly expressed endmembers that might be undetected if fewer iterations were completed. Since the oil spill pixels are expected to be relatively rare over the full image (compared to the total number of image pixels) and expected to be found presumably along the coastline of Barataria Bay landforms, a sufficiently large number of iterations was specified for the processing of all AVIRIS images. Therefore, the number of iterations was set to 50,000 in order to increase the probability of detecting spectrally-unique materials. PPI yields a map of how often a pixel was identified as being the most spectrally pure during all of PPI iterations, and a plot which indicates the total number of pixels recorded as extreme. Figure 14 illustrates the results of PPI calculations, where the number of pixels marked as spectrally extreme is plotted as a function of PPI iteration, and where the PPI threshold was set to 2.5, and the total number of iterations was set to 50,000. The cumulative number of pixels that was found to be spectrally extreme was 4,156 pixels for the AVIRIS image 1. For the second, third and fourth AVIRIS images, 5,976 pixels, 2,342 pixels, and 3,057 pixels were designated as spectrally-extreme/pure, respectively.

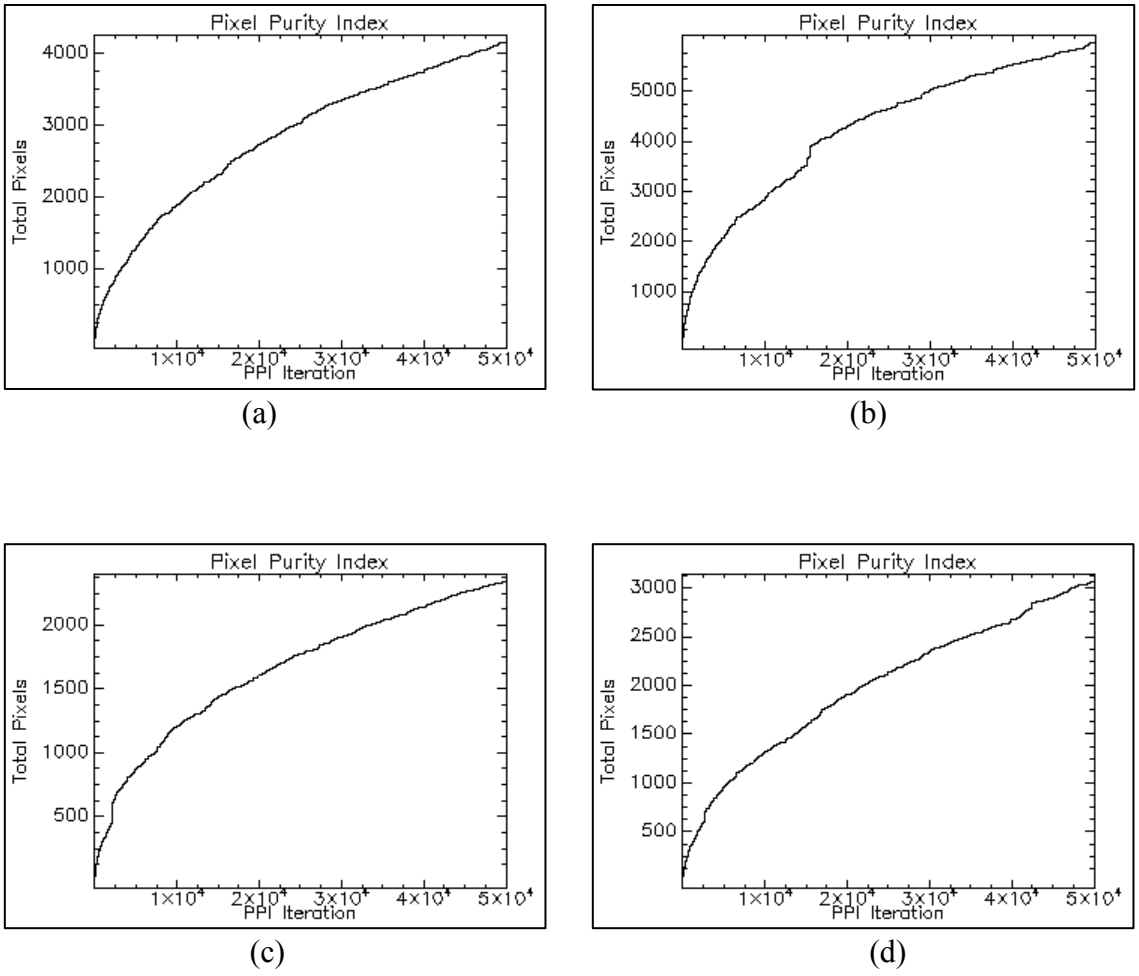

Figure 14 Pixel Purity Index plots derived from AVIRIS image processing. a), b), c) and d) give the PPI results by iteration for the first, second, third and fourth AVIRIS images, respectively.

More likely endmember pixel candidates can be identified by thresholding the PPI image. The aim of this research is to detect oiled vegetation likely associated with the Deepwater Horizon accident along the coastline of Gulf of Mexico; it is expected that the number of oiled pixels recorded as extreme by PPI will be relatively low compared to the number of pixels representing other features in the AVIRIS images. In

an attempt to detect these relatively rare pixels, it was empirically-determined that a PPI threshold value of 15 was sufficient to detect oiled pixels over the AVIRIS images. As a result of this threshold, a total of PPI 453 pixels were selected for further processing out of 4,156 pixels for AVIRIS image 1. The pixels that were determined as being the most spectrally pure based on thresholding were then treated as input to the *n*-Dimensional Visualizer, which is an interactive tool to select endmembers in *n*-space. The *n*-D Visualizer constitutes a final step in the ENVI endmember-extraction process; executing this step in a manual manner is relatively subjective in nature. Therefore, automatic clustering was performed at this stage to obtain the purest pixel signatures, and 20 endmember spectra were identified using the *n*-D Visualizer in this manner based on AVIRIS image 1. As noted in the methodology section, the number of endmembers that can be extracted from an image is usually taken as being the number MNF transform bands (or the inherent dimensionality of the data set) +1. Thus, a total of 20, 15, 24, and 20 endmembers were extracted from the first, second, third and fourth AVIRIS images, respectively.

Once the endmembers were extracted from the AVIRIS subimages, they were then manually labeled based on convergence of evidence from various sources. The sources of reference information used for endmember labeling include spectral signature characteristics of various materials from the literature, proximity to SCAT oil class areas, dissolved organic carbon (DOC) concentration values that fall within/nearby the same class as the endmember, and NAIP aerial orthophotographs. Kokaly *et al.* (2013) collected DOC concentration data at 10 oiled and 2 non-oiled sites in the Barataria Bay

area during 24-26 August 2010. A shapefile was created containing those DOC sampling points and associated DOC concentrations. Natter *et al.* (2012) noted that high DOC levels could be caused by oil components and/or increased organic substances released by microbial activities fueled by oil. The DOC concentrations for visibly-oiled sites ranged from 6.1 to 19.5 mg/L DOC, whereas the DOC concentrations at visibly-unoiled sites ranged from 8.4 to 9.1 mg/L DOC (Kokaly *et al*., 2013). Therefore the DOC concentrations greater than 9.1 mg/L DOC was used as threshold to decide whether the given site was oiled. As DOC concentrations increase at a given site, it is assumed for this research that that site entails a higher oil content compared to a sample location with a lower DOC concentration. In this research, these data were utilized as a type of evidence regarding the degree of oil present at a site during the endmember-labeling process. As part of this process, each spectral signature pertaining to land features were also compared with the spectral profiles of healthy marsh vegetation and oiled vegetation provided in Kokaly *et al.* (2013). As already demonstrated by Cloutis (1989), hydrocarbon-bearing reference objects are characterized by absorption maxima at 1730 and 2310 nm. These absorption peaks are typical of the C-H stretch: in particular, 1730 nm is the C-H stretch of the first Overtone band, and 2310 nm is the C-H stretch combination band. Therefore, in order to label an endmember, first, a given spectral profile was analyzed as to whether it contains any absorption peaks due to oil contamination. The spectral profiles from Kokaly *et al.* (2013) were thus also taken into account in order to compare the similarities of endmember profiles from *n*-D Visualizer. The coordinates of the pixels which are selected as extreme by *n*-D Visualizer are

located in the aerial photographs and the SCAT map in order to obtain any supporting evidence to label endmember spectral profiles correctly (e.g., as oiled marsh, marsh vegetation, etc.). If a given point was located along the coastline, endmember labeling was relatively straight forward compared with points falling within interior portions of coastal landforms since SCAT maps were produced according to *in situ* data collected along the shoreline of the Gulf of Mexico (Michel *et al.*, 2013). In order to label the points located in the interior marshland areas, endmember spectral profiles were analyzed as to whether or not oil absorption features are present. If a given endmember profile does not contain absorption features consistent with oiled material spectra, then it is labeled after checking the endmember coordinates with respect to the SCAT map, proximity to DOC sample points, and the aerial photographs. The oiled dry marsh class represents senescent or non-green vegetation since the endmember spectrum of oiled dry marsh does not appear as healthy vegetation spectra. This may be due to the following reasons: exposure to a large amount of oil, the type of oil, and/or the type of vegetation. Figure 15 (a) gives a spectral profile for potentially oil-impacted vegetation which has two absorption peaks around 1730 and 2310 nm. Comparison of the AVIRIS image-derived endmembers in the present study with spectra given in Kokaly et al. (2013) also provides similarities regarding absorption features.

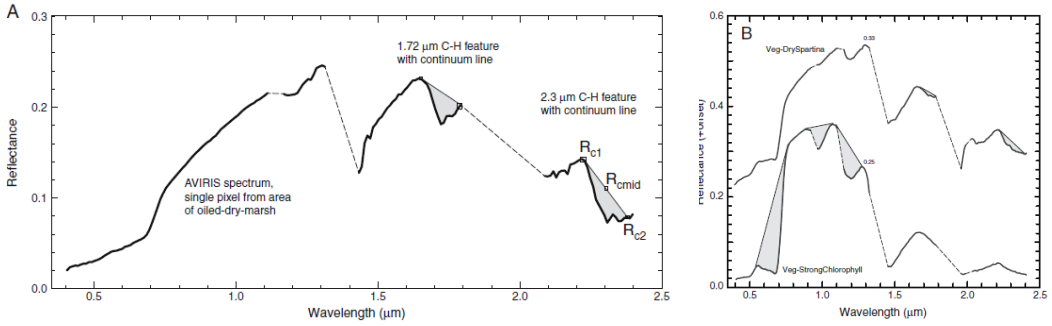

Figure 15 Reference spectra of (a) oiled dry marsh and (b) non-oiled vegetation (Source: Kokaly *et al.* (2013))

In addition, NAIP aerial orthophotographs also provide high-spatial resolution information regarding the presence or absence of dark (likely oiled) patches spatially coincident with endmember locations. Thus, the endmember labeled as oiled dry marsh was identified with evidence of oil-spill contamination according to the SCAT map, aerial photographs, and ancillary data from the literature. However, endmember spectra for light-oiled marsh vegetation present as relatively healthy vegetation, though they also entail oil-absorption features centered near 1.7 and 2.3 µm. Therefore, such spectra are labeled as light-oiled vegetation. Only for AVIRIS image 4 were medium- and heavy-oiled vegetation endmembers identified due to deeper absorption features of oil, and the location of the endmembers, which fall within or nearby the corresponding (medium- and heavy-oiled) SCAT classes. Along the coastline of the study area, there are mixed pixels which may a combination of water/vegetation or water/oil or water/vegetation/oil. The reflectance spectra of mixed pixels do not look like healthy or senescent vegetation. Thus, this class was named as Mixed (oil/water/vegetation). Multiple endmembers were identified for several classes because of inherent within-class spectral variability. For

instance, after identifying wetland vegetation spectra, they were labeled as wetland vegetation 1 class, where that type of wetland veg has a high reflectance in a certain portion of the spectrum, and wetland vegetation 2 class, where that type of wetland veg has a lower reflectance in that same portion of the spectrum. Pre-accuracy assessment, a merging process was applied for each class type with multiple endmember. In summary, endmembers were labeled according to proximity to DOC sample points (with associated DOC concentration values), visual interpretation of aerial photographs regarding oiled-vegetation presence, and the SCAT oil-class map. As noted in the Discussion, some degree of subjectivity exists in the endmember-labeling process.

Across all four AVIRIS subimages, there were 30 total endmembers that were collected to represent the wetland vegetation, including dry marsh. There are several pixels that contain mixed features, such as water/vegetation or water/oil or water/oil/vegetation, which may be an artifact of the water-masking process. Thus 21 total endmembers were selected to represent the mixed (oil/water/vegetation) class across all four AVIRIS subimages. Fourteen (14) and eleven (11) endmembers were selected to represent oiled dry mash and light oiled vegetation across all four AVIRIS images with the criteria of the oil existence on the given site in aerial photo, oil absorption features, and oil class map of SCAT, respectively. Only two (2) and one (1) endmembers were identified and labeled as medium- and heavy-oiled vegetation classes in the fourth AVIRIS image, respectively where the dominant criterion used for labeling these spectra was the SCAT map. Figure 16 (a)-(d) illustrates the extracted endmember

spectral signatures for the four AVIRIS subimages analyzed in this research, and Figure 17 (a)-(f) illustrates the surface reflectance spectra of each endmember within the scene.

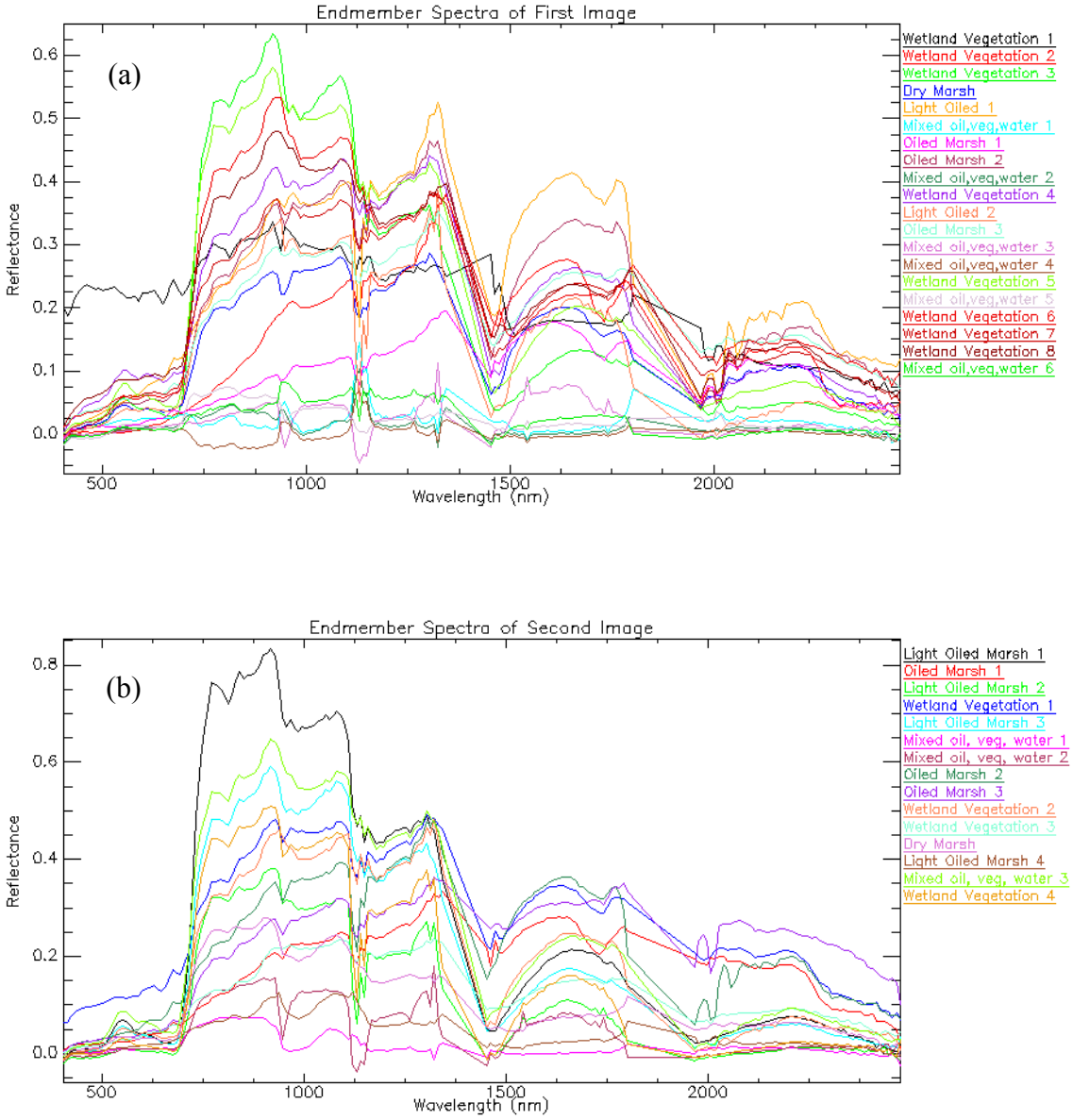

Figure 16 Extracted endmember spectra for a) AVIRIS image 1; b) AVIRIS image 2; c) AVIRIS image 3; d) AVIRIS image 4, which used as input to SID, MTMF and MESMA algorithms.

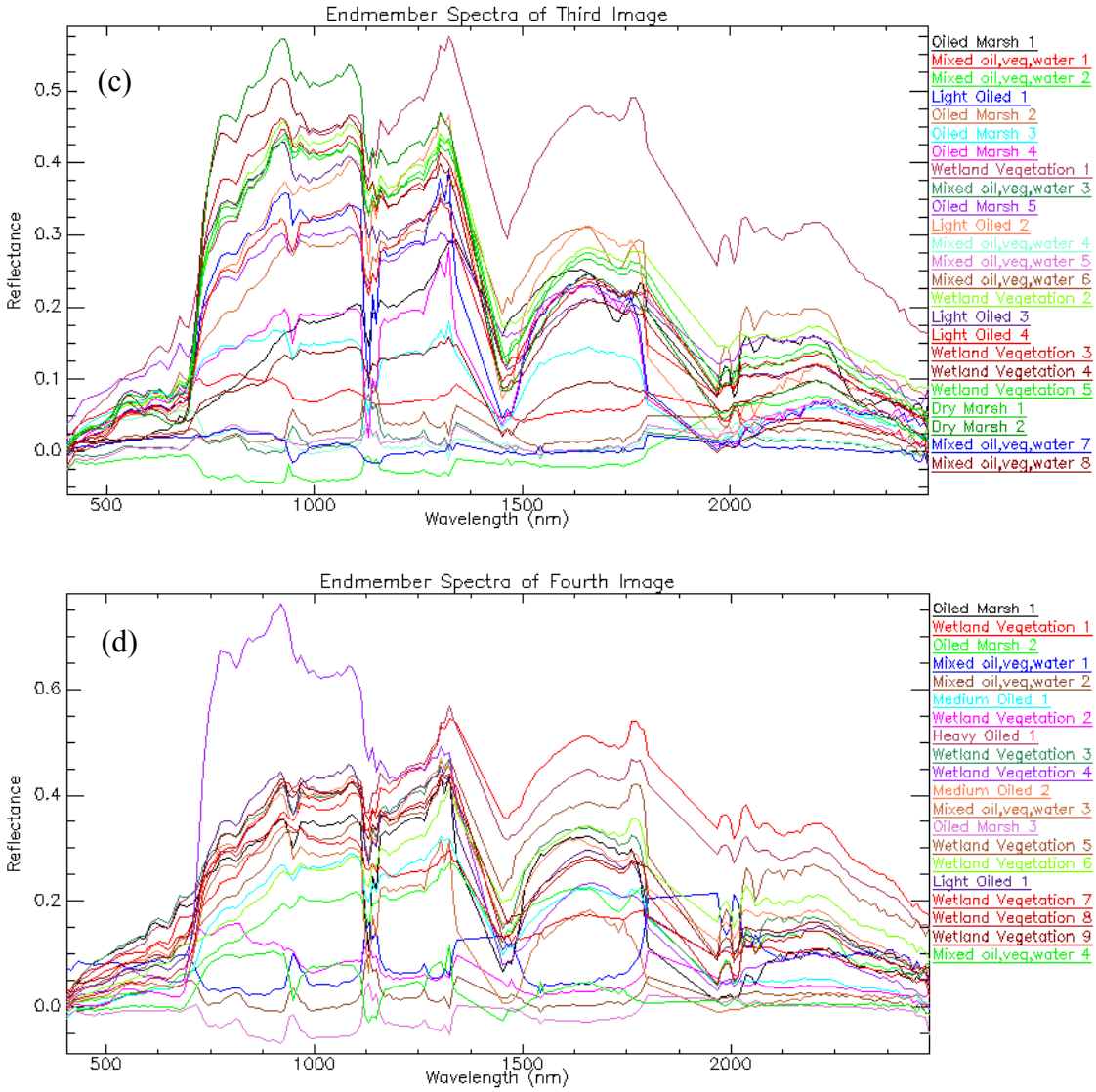

Figure 16 Continued

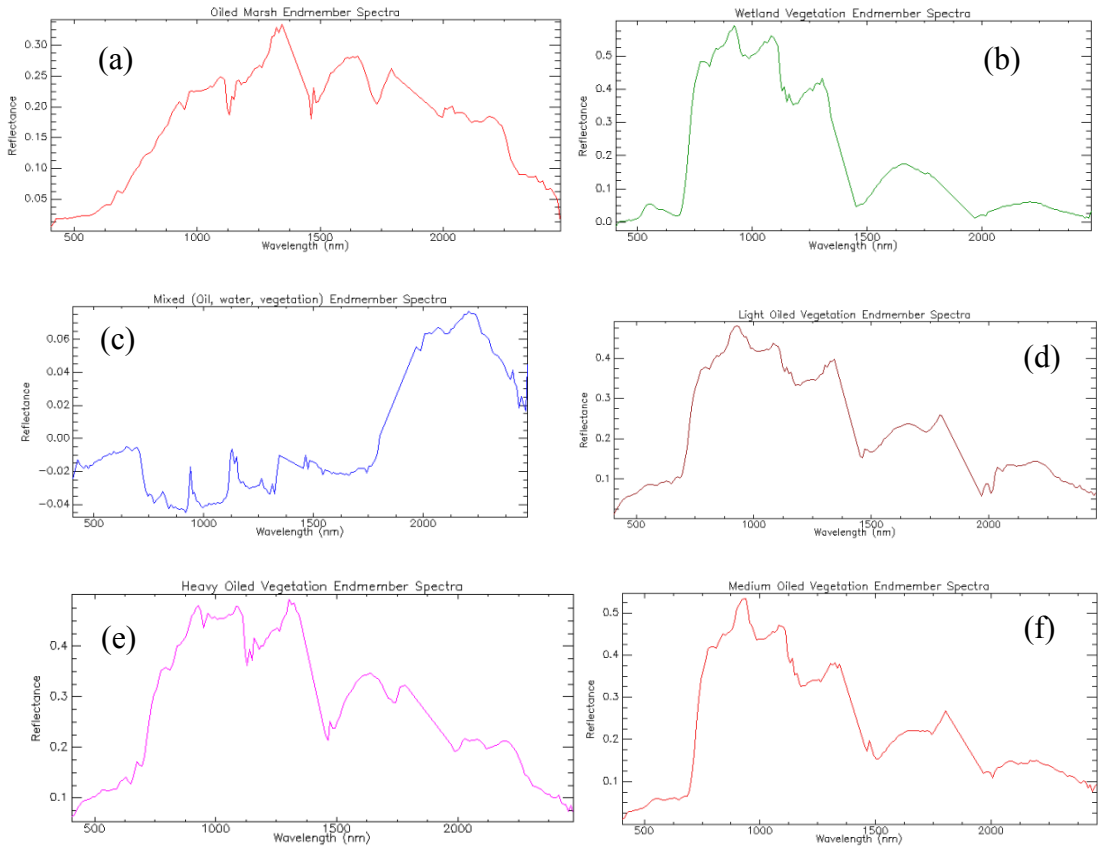

Figure 17 Endmember spectra of six classes used in classification: a) oiled dry marsh; b) wetland vegetation; c) mixed; d) light-oiled vegetation; e) heavy-oiled vegetation; and f) medium-oiled vegetation.

4.4 Classification Algorithms

Once all endmember-extraction and labeling processes were completed, labeled endmembers were mapped using the SID, MTMF, and MESMA algorithms. The performances of these classification algorithms are compared in terms of user's accuracy, producer's accuracy, overall accuracy, and Kappa coefficient of the resultant classified images in the accuracy assessment chapter (Chapter V), and some observations regarding computational efficiencies are also made.

4.4.1 Spectral Information Divergence (SID)

Spectral information divergence (SID) classification method was performed on the geometrically- and atmospherically-corrected hyperspectral spatial-subset images. SID is based on quantifying spectral similarities by using a predetermined reference spectrum. Several different thresholds were analyzed, and an optimized SID threshold value of 0.07 provided the best result in terms of minimizing the number of unclassified pixels within the hard classified image. The input image to the classifier was a masked image, but the mask should be specified/applied to the image during execution of the algorithm. Otherwise, the output classification map does not provide reasonable results. Once the SID output map was created, the endmembers that were labeled as dry marsh and healthy vegetation were merged together into a single class referred to as marsh vegetation. The subclasses of light-oiled vegetation were labeled as light-oiled

vegetation 1, light-oiled vegetation 2, and so on, due to differences in reflectance properties. Those subclasses were merged prior to classification. The same labeling and merging procedure was also performed for the mixed (oil/water/vegetation) and oiled dry marsh subclasses for each subimage independently. The output map of the SID classification results is shown in Figure 18. Mixed pixels including, water, marsh vegetation and/or oil are displayed in blue. The green color represents the marsh vegetation, whereas light-oiled vegetation is displayed in yellow, and oiled dry marsh vegetation is displayed in red. The colors assigned for each class are consistent across all hard classification maps. Results demonstrate that oiled dry marsh vegetation was observed along the coastlines of Bay Jimmy, Bay Chene Fleur, and Wilkinson Bay, even though some oiled dry marsh and light-oiled pixels are misclassified in the marshland area.

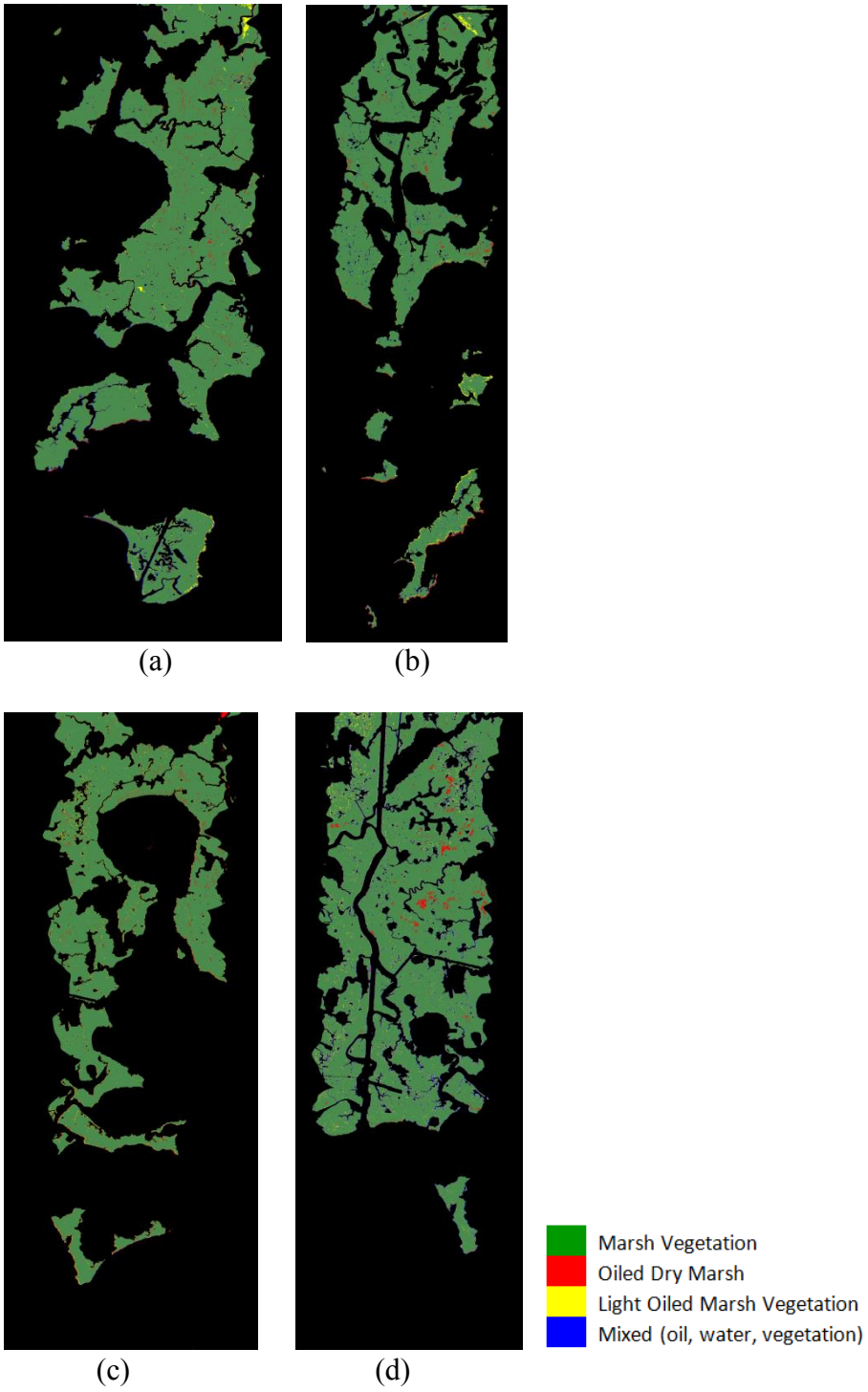

Figure 18 Hard classified images based on the SID classifier: a) AVIRIS image 1; b) AVIRIS image 2; c) AVIRIS image 3; d) AVIRIS image 4.

4.4.2 Mixture Tuned Matched Filterinig (MTMF)

Mixture tuned matched filtering (MTMF) has been reported as a superior method relative to some other methods for detection of various materials in hyperspectral images (Boardman, 1998). The Mixture Tuned Matched Filtering algorithm consists of two phases; a Matched Filter calculation for abundance estimation and a Mixture Tuning calculation for the identification and rejection of false positives. MTMF method was performed on the MNF transformed data. For each endmember, MTMF produces one MF image and one infeasibility image. The output MF score and infeasibility images sets are utilized as input to a rule classifier in order to generate a hard MTMF classified image for a given subscene. Pixels with high MF and low infeasibility values are the most suitable values for accurately defining a class.

MTMF AVIRIS-image-derived fractional abundance images were created via interactive stretching. Abundance estimates for marsh vegetation, oiled dry marsh, light-oiled vegetation and mixed (oil/water/vegetation) endmembers are shown in Figure 19 as grayscale images. Brighter pixels in the abundance images represent endmembers with higher fractional abundances. For this visualization, the abundance image of marsh vegetation was stretched between 0.1 and 0.4, light-oiled vegetation was stretched between 0 and 0.68, oiled dry marsh was stretched between 0 and 0.7, and mixed (oil, water, vegetation) was stretched between 0 and 0.42.

Maps can be produced from MTMF results by selecting hard thresholds for the target classes from a graphics display of MF score versus infeasibility score (Boardman,

1998). Thus, MF and infeasibility images values are evaluated using scatterplots of MF score versus infeasibility value. Due to the subjectivity of this mapping method, several thresholds are identified via trial-and-error based on the scatterplots and tested on AVIRIS Image 1. Based on this experimentation, the MF score threshold was set at 0.4, and the infeasibility threshold was set at 4.00 across all AVIRIS images. Note that the color assignments for different classes in the MTMF-based classified images are identical to those of SID—i.e., red for oiled dry marsh; yellow for light-oiled vegetation; blue for mixed (oil/water/vegetation); and green for marsh vegetation. As potentially evident in Figure 20, there are many misclassified pixels across the AVIRIS images (which is quantitatively assessed at the classification accuracy-assessment stage). The hard classification images demonstrate that light-oiled vegetation, mixed (oil/water/vegetation), and oiled dry marsh classes were confused with the marsh vegetation class.

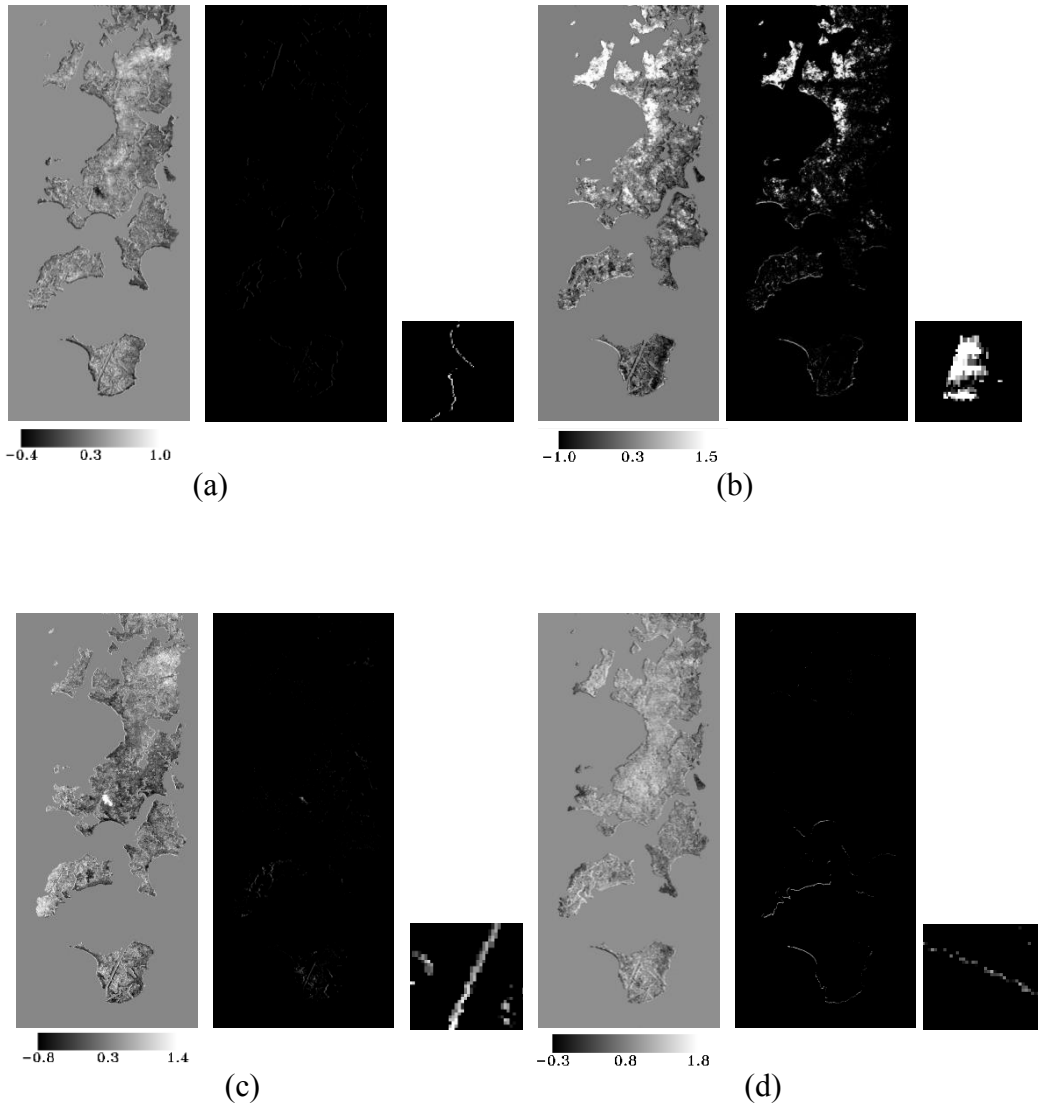

Figure 19 MTMF-based fractional abundance images for a) light-oiled vegetation; b) marsh vegetation; c) mixed (oil/water/vegetation); and d) oiled dry marsh.

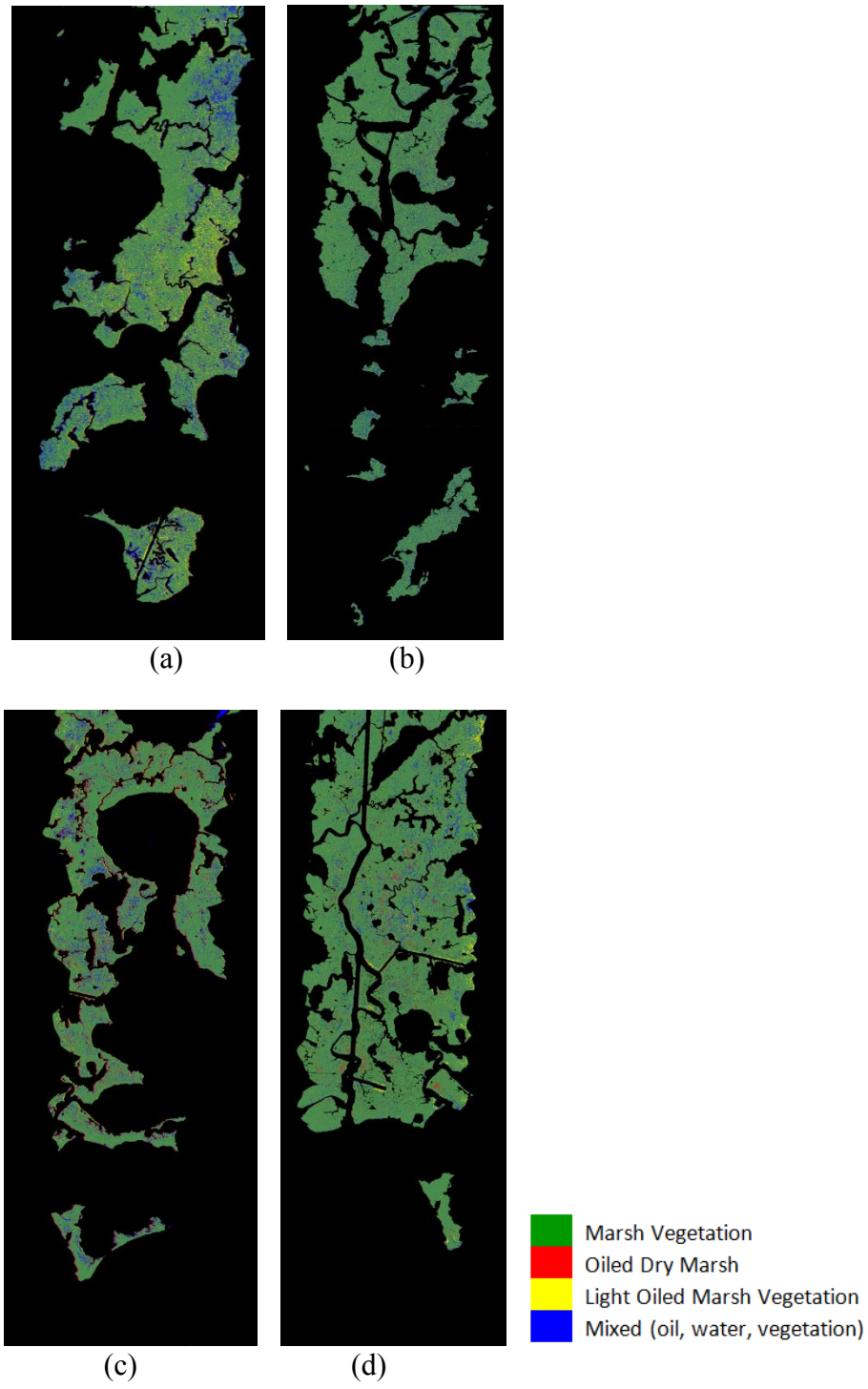

Figure 20 The hard classified images based on MTMF classification: a) AVIRIS image 1; b) AVIRIS image 2; c) AVIRIS image 3; and d) AVIRIS image 4.

4.4.3 Multiple Endmember Spectral Mixture Analysis (MESMA)

In this research, MESMA was applied to map potentially oiled vegetation using AVIRIS hyperspectral data acquired after the Deepwater Horizon accident in Gulf of Mexico. An open-source plug-in for the ENVI™ software, referred to as Visualization and Image Processing for Environmental Research (VIPER) Tools (Roberts *et al*., 2007), was used to apply MESMA to these AVIRIS images. The atmospherically-corrected land-only AVIRIS images were used as input to the MESMA algorithm. Before applying MESMA, a given endmember set was specified as inputs as ROIs. The endmember file for AVIRIS image 1 contains 20 endmembers, representing materials within the image including oiled dry marsh vegetation, marsh vegetation, light-oiled vegetation, and mixed (oil/water/vegetation) classes.

The VIPER Tools software used in this study allowed for fixing the minimum and maximum allowable fraction values; the maximum allowable shade fraction value; and the maximum allowable RMSE in obtaining MESMA classification images via application to the AVIRIS images. For the minimum allowable endmember fraction, thresholds can range from -0.5 to 1. For the maximum allowable endmember fraction, thresholds can range from 1 to 1.5. The threshold values of maximum shade fraction can range from 0 to 1. In this research, the minimum allowable endmember fraction, maximum allowable endmember fraction, and maximum allowable shade fraction were set to values of −0.30, 1.40, and 0.95, respectively for all images. In this study, 2- and 3-endmember models were investigated in order to determine the best classification result.

However, Powell *et al.* (2007) note that the total number of endmembers in the potential models is inversely proportional to the computational efficiency and accuracy. Likewise, various studies demonstrate that 4-endmember models do not necessarily provide better performance than 3-endmember models (Fitzgerald *et al.*, 2005; Powell *et al.*, 2007). In this research, it was empirically-determined that 2-endmember models provide the best classification result.

Figure 21 illustrates the results of MESMA hard classification as zoomed-in subimages, and the corresponding zoomed-in subsets of NAIP aerial orthophotographs containing dark patches, in order to provide a visual comparison between reference and classified data. MESMA-derived hard classified images are given in Figure 22. Patterns of MESMA-based classified pixels can be compared with those derived from SID and MTMF.

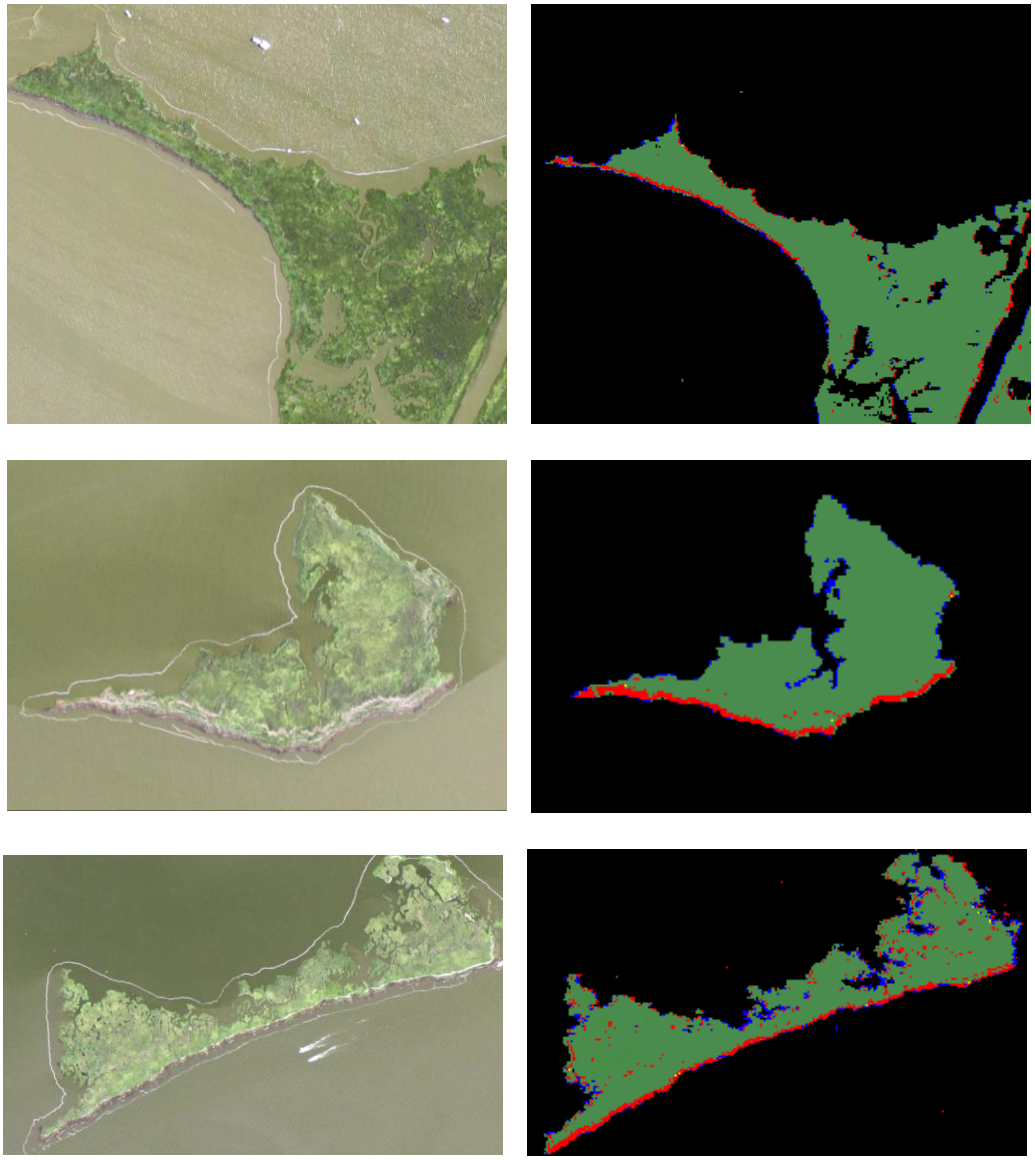

Figure 21 Zoomed-in/magnified subsets of NAIP aerial orthophotographs containing dark patches (left) and zoomed-in image subsets of MESMA hard classification images (right), with vegetation in green, oiled dry marsh in red, and mixed (oil/water/vegetation) in blue color.

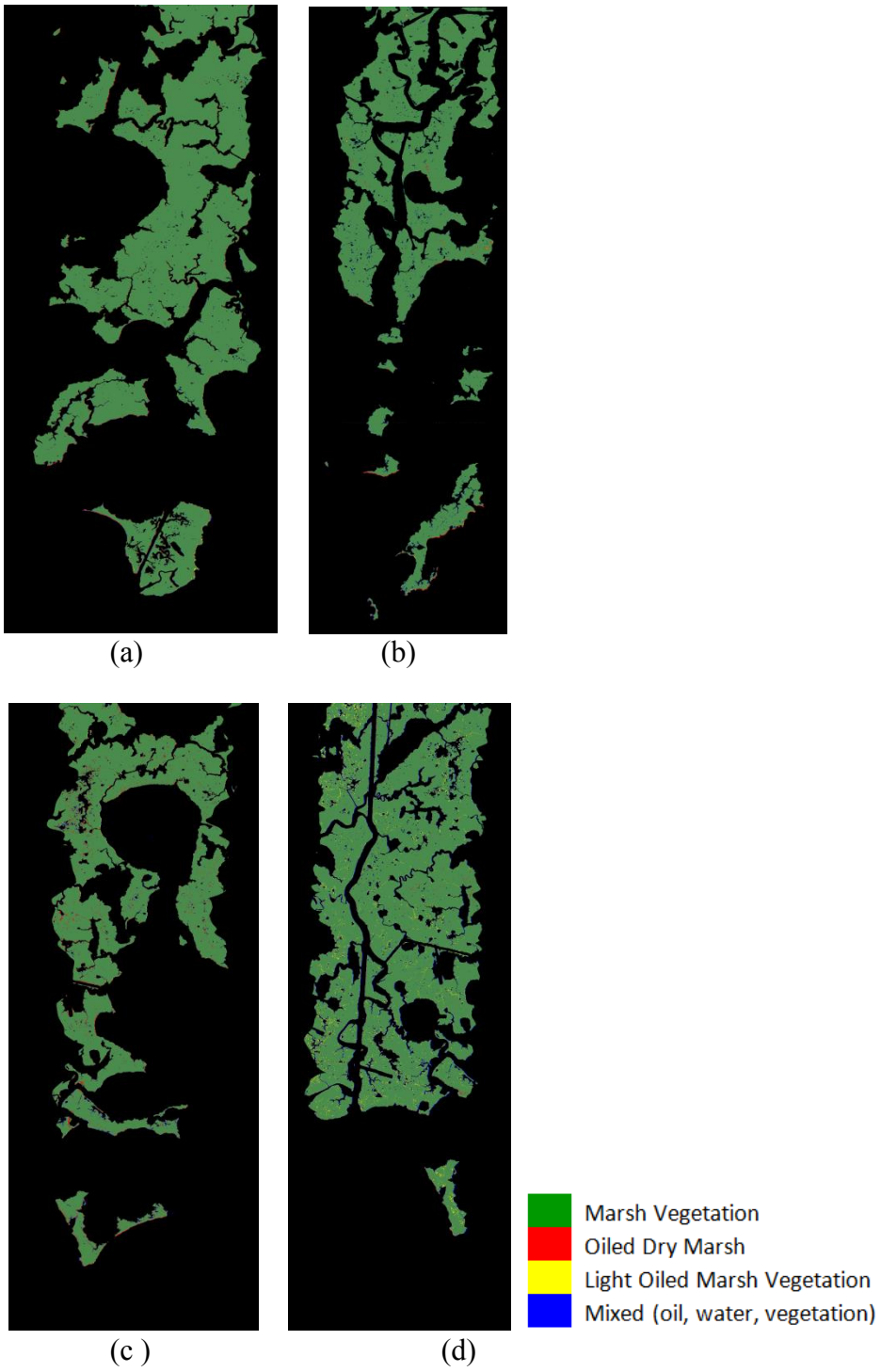

Figure 22 Hard classified images derived from the MESMA algorithm: a) AVIRIS image 1; b) AVIRIS image 2; c) AVIRIS image 3; d) AVIRIS image 4.

CHAPTER V

ACCURACY ASSESSMENT

Results of three tested classification methods are evaluated in terms of their capacity to detect oiled vegetation along the coastline of the Gulf of Mexico and adjacent terrestrial environment via hard classification accuracy assessments.

For the purpose of validation, 50 stratified random sample points per class were generated for each classification accuracy assessment. The classifications derived from AVIRIS images 1, 2, and 3 consist of four classes, translating to a total of 200 stratified random accuracy-assessment points per image (Congalton, 1991). Classified images derived from AVIRIS image 4 contain six classes; thus, a total of 300 stratified random accuracy-assessment points per classified image were employed in the evaluation of the image 4 results. The accuracy assessments were performed by comparing algorithm-derived classification values associated with the randomly-selected pixels with the reference data. Three sources of reference data were utilized in the construction of the error matrices: (1) SCAT map which provides field-based observations of the degree of oil accumulation along the coastline; (2) high-spatial resolution aerial photographs acquired before and after the oil spill; and (3) *in situ* measurements taken from the literature. Once all the points for each class were compared with the reference data, the total number of correctly-classified and misclassified points was calculated. As shown in Tables 3-6, the error matrix was used to summarize the results of accuracy assessment by comparing the classification results with the reference data. The user's accuracy

(errors of commission) and producer's accuracy (errors of omission) for each class, as well as the overall accuracy, were reported in the error matrix (Congalton, 1991). The error matrix columns represent the ground reference values, and the rows contain the class values.

The user's accuracy is a map-based accuracy which refers to the probability that a pixel labeled as a certain land-cover class in the map is really put into this class in the classification image. It is calculated from the rows of the confusion matrix by counting total number of correct points in a class and dividing by the sum of total number of pixels in the rows. The producer's accuracy is a reference-based accuracy which refers to the probability that a certain land-cover on the ground is classified as such. It is calculated from the columns of the confusion matrix by counting total number of correct points in a class and dividing by the sum of the total number of pixels in the column. Overall classification accuracy was calculated from this table by counting how many pixels were classified the same in the remote-sensing image and on the ground and dividing this by the total number of pixels (Congalton, 1991).

In addition, the Kappa coefficient is computed for each classified image, and these values are summarized in Table 7, along with overall accuracy values. The Kappa coefficient provides an overall agreement between the remote-sensing classification and the reference data by taking non-diagonal cells into account, in addition to diagonal cells (Congalton 1991).

Error matrices were generated for each classification method over the four AVIRIS images classified. Table 3 (a)-(c) gives the error matrices for AVIRIS image 1

accuracy assessments, which summarize the overall accuracy, producer's accuracy, and user's accuracy computed from the SID, MTMF, and MESMA classifications, respectively. According to Table 3, oiled dry marsh vegetation, mixed (oil/water/vegetation), light-oiled marsh vegetation, and marsh vegetation classes achieved an overall classification accuracy of 83.5% and a Kappa coefficient of 0.78 via MESMA, whereas the overall accuracies of the MTMF and SID classifications were 52.5% and 71.5%, respectively, with Kappa coefficient values of 0.39 and 0.62, respectively. MTMF accuracy assessment results reveal that there are many confused and misclassified pixels in all classes with low producer's accuracy and user's accuracy while the results of MESMA show high accuracy for misclassified pixels. Regarding producer's accuracy, the oiled dry marsh and light-oiled vegetation were mapped with high producer's accuracy values and were consistent across all images in terms of MESMA results. The producer's accuracies of the MTMF- and SID-classified images are lower than that of MESMA. Oiled dry marsh and light-oiled vegetation are confused with marsh vegetation, particularly with the MTMF classification.

Table 4 (a)-(c) gives the error matrices for AVIRIS image 2 accuracy assessments, which summarizes overall accuracy, producer's accuracy, and user's accuracy calculated from the SID, MTMF, and MESMA classifications, respectively. The hard classification results for AVIRIS image 2 derived from the SID, MTMF and MESMA algorithms entail overall accuracies ranging from 54.5% to 78.5%. The results indicate that MESMA classification accuracy is the highest for this image, with an overall accuracy of 78.5 %, whereas the overall accuracies of MTMF and SID

classification techniques are 54.5% and 70.5%, respectively, with Kappa coefficients of 0.37 and 0.60, respectively. MTMF mostly misclassified marsh vegetation pixels as oiled dry marsh, mixed (water/oil/vegetation) and light-oiled vegetation. This confusion may occur because of the spectral similarity of classes with other endmember reference spectra.

Table 5 (a)-(c) gives the error matrices for AVIRIS image 3 accuracy assessments, which summarize overall accuracy, producer's accuracy, and user's accuracy computed from the SID, MTMF, and MESMA classifications, respectively. MESMA performed with the highest overall accuracy (79%) and Kappa coefficient (0.72), and MTMF yielded the lowest overall accuracy (50.5%) and Kappa coefficient (0.34). Improvements were noted in producer's accuracy of the oiled dry marsh class and light-oiled vegetation with the MESMA classification compared with MTMF results for this image. Producer's and user's accuracies for all land-cover classes were also higher for MESMA, relative to those derived from the other classification methods.

Table 6 (a)-(c) gives the error matrices for AVIRIS image 4 accuracy assessments, which summarize overall accuracy, producer's accuracy, and user's accuracy computed from the SID, MTMF, and MESMA classifications, respectively. Different than the first three AVIRIS images, the fourth AVIRIS image contains six (6) classes total, enabling mapping of heavy-oiled vegetation and medium-oiled vegetation, as endmembers corresponding to those classes can be identified during the endmember-labeling process. Therefore, the overall accuracies of the classifications were expected to be lower than those of the first three images due to the increase in the number of classes.

Accuracy-assessment results reveal that MESMA produced the most accurate results in terms of user's and producer's accuracies for oiled dry marsh and light-oiled classes, whereas MTMF generated the least accurate results. In the AVIRIS image, some spectral and spatial overlap likely exists in the medium-oiled, heavy-oiled, and light-oiled vegetation, which may also translate to spectral similarity of these endmembers.

MESMA classification approach provides the best performance (highest classification accuracies) in detecting oiled vegetation along the coastline and in a terrestrial environment, whereas SID provides slightly lower overall classification accuracies compared to MESMA, and MTMF yields the lowest overall accuracy across all images. Compared to MTMF, SID and MESMA approaches produce a more accurate representation of oiled vegetation and marsh vegetation classes. The fact that MESMA enables the number and types of endmembers to vary on a per-pixel basis likely contributes to its performance in this domain. Also, these results demonstrate that hyperspectral images can be utilized successfully to identify oiled vegetation in a coastal terrestrial environment with appropriate classification algorithms.

Table 3 Error matrices for AVIRIS image 1, showing overall accuracy, producer's accuracy, and user's accuracy calculated for the three classification techniques investigated: a) SID; b) MTMF; and c) MESMA algorithm results.

(a)

		Reference					
	Class Name	Oiled Marsh Veg	Mixed oil, water, veg	Light Oiled Marsh Veg	Marsh Veg	Total	User's Accuracy (%)
Classified	Oiled Marsh Veg	**34**	3	3	10	50	68
	Mixed Oil, Water, Veg	0	**26**	0	24	50	52
	Light Oiled Marsh Veg	2	1	**28**	9	50	76
	Marsh Veg	1	2	2	**45**	50	90
	Total	37	32	43	88	200	
	Producer's Accuracy (%)	91.89	81.25	88.37	51.14		
	Overall Accuracy (%)	**71.5**					

(b)

		Reference					
	Class Name	Oiled Marsh Veg	Mixed oil, water, veg	Light Oiled Marsh Veg	Marsh Veg	Total	User's Accuracy (%)
Classified	Oiled Marsh Veg	**21**	5	5	19	50	42
	Mixed Oil, Water, Veg	8	**25**	6	11	50	50
	Light Oiled Marsh Veg	6	5	**21**	18	50	42
	Marsh Veg	4	3	5	**38**	50	76
	Total	39	38	37	86	200	
	Producer's Accuracy (%)	53.85	65.79	56.76	44.19		
	Overall Accuracy (%)	**52.5**					

(c)

		Reference					
	Class Name	Oiled Marsh Veg	Mixed oil, water, veg	Light Oiled Marsh Veg	Marsh Veg	Total	User's Accuracy (%)
Classified	Oiled Marsh Veg	**38**	2	1	9	50	76
	Mixed Oil, Water, Veg	2	**42**	4	2	50	84
	Light Oiled Marsh Veg	0	4	**41**	5	50	82
	Marsh Veg	2	1	1	**46**	50	92
	Total	42	49	47	62	200	
	Producer's Accuracy (%)	90.48	85.71	87.23	74.19		
	Overall Accuracy (%)	**83.5**					

Table 4 Error matrices for AVIRIS image 2, showing overall accuracy, producer's accuracy, and user's accuracy calculated for the three classification techniques investigated: a) SID; b) MTMF; and c) MESMA algorithm results.

(a)

		Reference					
	Class Name	Oiled Marsh Veg	Mixed oil, water, veg	Light Oiled Marsh Veg	Marsh Veg	Total	User's Accuracy (%)
Classified	Oiled Marsh Veg	**28**	2	5	15	50	56
	Mixed Oil, Water, Veg	8	**38**	0	4	50	76
	Light Oiled Marsh Veg	0	2	**31**	17	50	62
	Marsh Veg	1	0	5	**44**	50	82
	Total	37	42	41	80	200	
	Producer's Accuracy (%)	75.68	90.48	75.61	55		
	Overall Accuracy (%)	**70.5**					

(b)

		Reference					
	Class Name	Oiled Marsh Veg	Mixed oil, water, veg	Light Oiled Marsh Veg	Marsh Veg	Total	User's Accuracy (%)
Classified	Oiled Marsh Veg	**22**	8	2	18	50	44
	Mixed Oil, Water, Veg	4	**27**	5	14	50	54
	Light Oiled Marsh Veg	4	3	**24**	19	50	48
	Marsh Veg	5	7	2	**36**	50	72
	Total	35	45	33	87	200	
	Producer's Accuracy (%)	62.86	60	72.73	41.33		
	Overall Accuracy (%)	**54.5**					

(c)

		Reference					
	Class Name	Oiled Marsh Veg	Mixed oil, water, veg	Light Oiled Marsh Veg	Marsh Veg	Total	User's Accuracy (%)
Classified	Oiled Marsh Veg	**34**	1	1	14	50	68
	Mixed Oil, Water, Veg	0	**41**	0	9	50	82
	Light Oiled Marsh Veg	0	3	**36**	11	50	72
	Marsh Veg	1	0	3	**46**	50	92
	Total	35	45	40	80	200	
	Producer's Accuracy (%)	97.14	91.11	90	57.5		
	Overall Accuracy (%)	**78.5**					

Table 5 Error matrices for AVIRIS image 3, showing overall accuracy, producer's accuracy, and user's accuracy calculated for the three classification techniques investigated: a) SID; b) MTMF; and c) MESMA algorithm results.

(a)

		Reference					
	Class Name	Oiled Marsh Veg	Mixed oil, water, veg	Light Oiled Marsh Veg	Marsh Veg	Total	User's Accuracy (%)
Classified	Oiled Marsh Veg	**27**	2	2	19	50	54
	Mixed Oil, Water, Veg	5	**36**	3	6	50	72
	Light Oiled Marsh Veg	7	2	**29**	12	50	58
	Marsh Veg	0	1	4	**45**	50	90
	Total	39	41	38	82	200	
	Producer's Accuracy (%)	69.23	87.8	76.32	54.88		
	Overall Accuracy (%)	**68.5**					

(b)

		Reference					
	Class Name	Oiled Marsh Veg	Mixed oil, water, veg	Light Oiled Marsh Veg	Marsh Veg	Total	User's Accuracy (%)
Classified	Oiled Marsh Veg	**21**	8	4	17	50	42
	Mixed Oil, Water, Veg	4	**23**	1	22	50	46
	Light Oiled Marsh Veg	1	1	**28**	20	50	56
	Marsh Veg	7	9	5	**29**	50	58
	Total	33	41	38	88	200	
	Producer's Accuracy (%)	63.64	56.1	73.68	32.95		
	Overall Accuracy (%)	**50.5**					

(c)

		Reference					
	Class Name	Oiled Marsh Veg	Mixed oil, water, veg	Light Oiled Marsh Veg	Marsh Veg	Total	User's Accuracy (%)
Classified	Oiled Marsh Veg	**34**	3	1	12	50	68
	Mixed Oil, Water, Veg	0	**43**	1	6	50	86
	Light Oiled Marsh Veg	2	3	**35**	10	50	70
	Marsh Veg	1	1	2	**46**	50	92
	Total	37	50	39	74	200	
	Producer's Accuracy (%)	91.89	86	89.74	62.16		
	Overall Accuracy (%)	**79**					

Table 6 Error matrices for AVIRIS image 4, showing overall accuracy, producer's accuracy, and user's accuracy calculated for the three classification techniques investigated: a) SID; b) MTMF; and c) MESMA algorithm results.

(a)

		Reference							
	Class Name	Oiled Marsh Veg	Mixed oil, water, veg	Heavy Oiled	Medium Oiled	Light Oiled Marsh Veg	Marsh Veg	Total	User's Accuracy (%)
Classified	Oiled Marsh Veg	**29**	0	2	1	2	16	50	58
	Mixed Oil, Water, Veg	0	**31**	2	2	3	12	50	62
	Heavy Oiled	0	2	**29**	5	6	8	50	58
	Medium Oiled	0	0	1	**28**	6	15	50	56
	Light Oiled Marsh Veg	0	0	0	0	**31**	19	50	62
	Marsh Veg	1	3	1	0	2	**43**	50	86
	Total	30	36	35	36	50	113	300	
	Producer's Accuracy (%)	96.67	86.11	82.86	77.78	62.00	38.05		
	Overall Accuracy (%)	**63.67**							

(b)

		Reference							
	Class Name	Oiled Marsh Veg	Mixed oil, water, veg	Heavy Oiled	Medium Oiled	Light Oiled Marsh Veg	Marsh Veg	Total	User's Accuracy (%)
Classified	Oiled Marsh Veg	**19**	5	4	4	2	16	50	38
	Mixed Oil, Water, Veg	3	**22**	2	2	3	18	50	44
	Heavy Oiled	4	2	**9**	5	6	24	50	18
	Medium Oiled	0	3	5	**10**	6	26	50	20
	Light Oiled Marsh Veg	2	9	2	3	**14**	20	50	28
	Marsh Veg	1	6	1	2	6	**34**	50	68
	Total	29	47	23	26	37	138	300	
	Producer's Accuracy (%)	65.52	46.81	39.13	38.46	37.84	24.64		
	Overall Accuracy (%)	**36**							

(c)

		Reference							
	Class Name	Oiled Marsh Veg	Mixed oil, water, veg	Heavy Oiled	Medium Oiled	Light Oiled Marsh Veg	Marsh Veg	Total	User's Accuracy (%)
Classified	Oiled Marsh Veg	**32**	0	0	1	0	17	50	64
	Mixed Oil, Water, Veg	0	**37**	1	0	1	11	50	74
	Heavy Oiled	0	2	**34**	5	4	5	50	68
	Medium Oiled	0	2	0	**31**	3	14	50	62
	Light Oiled Marsh Veg	0	3	1	1	**35**	10	50	70
	Marsh Veg	1	2	0	0	1	**46**	50	92
	Total	33	46	36	38	44	103	300	
	Producer's Accuracy (%)	96.97	80.43	94.44	81.58	79.55	44.66		
	Overall Accuracy (%)	**71.67**							

Table 7 Comparison of accuracy measurements of SID, MTMF and MESMA approach

	SID		MTMF		MESMA	
	Overall Accuracy (%)	Kappa Coefficient	Overall Accuracy (%)	Kappa Coefficient	Overall Accuracy (%)	Kappa Coefficient
Image 01	71.50	0.62	52.50	0.37	83.50	0.78
Image 02	70.50	0.60	54.50	0.39	78.50	0.71
Image 03	68.50	0.58	50.50	0.34	79	0.72
Image 04	63.67	0.56	36.00	0.23	71.67	0.66

Table 8 Test for significant differences between error matrices for the classification algorithms for a) AVIRIS image 1; b) AVIRIS image 2; c) AVIRIS image 3; and d) AVIRIS image 4

(a)

Pairwise Comparison	Z Statistic	Result
SID and MTMF	3.5368	S
SID and MESMA	-3.2086	S
MTMF and MESMA	-6.9979	S

(b)

Pairwise Comparison	Z Statistic	Result
SID and MTMF	3.3186	S
SID and MESMA	-1.848	NS
MTMF and MESMA	-5.2015	S

(c)

Pairwise Comparison	Z Statistic	Result
SID and MTMF	3.6491	S
SID and MESMA	-2.4142	S
MTMF and MESMA	-6.0985	S

(d)

Pairwise Comparison	Z Statistic	Result
SID and MTMF	6.7860	S
SID and MESMA	-2.0996	S
MTMF and MESMA	-9.0349	S

S = Significant result at the 95% confidence level
NS = Non-Significant result at the 95% confidence level
SID = Spectral information divergence
MTMF = Mixture Tuned Matched Filtering
MESMA = Multiple Endmember Spectral Mixture Analysis

Significance testing was also performed in a pairwise manner between error matrices by computing a Z statistic. The Z statistic used to determine if the classification is significantly better than a random result. At the 95% confidence level, the critical value would be 1.96 (Congalton & Green, 2008). Therefore, if the absolute value of the test Z statistic is greater than 1.96, the result is significant and it means that the classification is better than random. Table 8 (a)-(d) present the pairwise tests for significant differences between contingency tables for all the classification algorithms. All MESMA results yielded significantly higher classification accuracies at the 95% confidence level than MTMF and SID results (with the exception of SID vs. MESMA for Image 2) with Z statistics from the pairwise comparisons ranging between -1.8 to -9.0. The results of the pairwise test for significance between MESMA and SID classification results are always significantly better than those of MTMF (at the 95% confidence level).

In conclusion, while single endmember classification algorithms, SID and MTMF, cannot account for considerable spectral variation within a class, MESMA can also account for within-class variability. Therefore most materials were mapped at relatively high accuracies via MESMA approach. MESMA improved the overall, user's and producer's classification accuracies compared to SID and MTMF across all AVIRIS subimages, since it is capable of minimizing spectral confusion.

CHAPTER VI

DISCUSSION AND CONCLUSION

An imaging spectroscopic approach was used to detect oiled vegetation along the Gulf of Mexico in southern Louisiana. FLAASH atmospheric correction, MNF transform, PPI image generation, and *n*-D Visualizer has been successfully performed to extract endmembers of target materials. AVIRIS hyperspectral image data collected over Barataria Bay, LA after the Deepwater Horizon oil rig accident have been analyzed with three different high-dimensional classification approaches, including SID, MTMF and MESMA. Regarding the identification of oiled vegetation, data analysis and accuracy assessment revealed that MESMA and SID performed well in identifying oiled marsh vegetation.

6.1 Discussion

This research focused on terrestrial oil-spill detection based on hyperspectral images. For this purpose, different remote-sensing image processing techniques were employed to identify oiled vegetation along the coastline of the Gulf of Mexico and in the marshland areas. Since all tasks performed in this research were interrelated to each other, the result from one step may affect the outcome of another step/method. Therefore, uncertainty or error associated with a given step could contribute to error in a

subsequent step. In this section, potential uncertainties of image processing throughout this research are discussed in order to improve classification accuracies of future studies.

One source of uncertainty lies with the masking process used. The majority of oil-impacted marsh vegetation was expected to be located along the coastline rather than the interior marshland areas. However, since detection of oil on the water surface was not the focus of the present research, a water mask (as well as associated boat and boat-wake masks) was created and applied. Due to (likely spatially-varying) inaccuracies associated with the thresholding step used for mask generation, some information loss regarding oil distribution along the shoreline may have occurred.

During the noise- and dimensionality-reduction process, specific output MNF bands were selected for further analysis based on the premise that they contain most of the information content in the data set. Although the AVIRIS image set was preprocessed carefully by creating masks and performing atmospheric correction, the number of output MNF images may not yield the best result in terms of subsequent endmember-extraction and classification. Furthermore, it is possible that other dimensionality-reduction methods could accrue better results.

There are several considerations regarding endmembers. First, field-derived endmembers can be used, in addition to image-derived endmembers, and the results could be compared in terms of accuracy. Endmembers derived from remote-sensor images were utilized in the present research. Since subjectivity can markedly enter into the endmember-extraction process, automatic clustering was performed to obtain the purest pixel signatures while minimizing analyst subjectivity. However, it is certainly

possible that optimal results may not be obtained in this manner, as some endmembers may be missed, and the technique may be sensitive to noise. Second, it is possible that more oiled-vegetation and healthy vegetation endmembers could be extracted from the images (e.g., if different dimensionality-reduction and/or endmember-extraction methods were used). Thus, more accurate classification results could potentially be accrued.

Some subjectivity was also part of the endmember-labeling process. The sources of reference information used for endmember labeling include spectral signature characteristics from the literature, proximity to SCAT oil class areas, dissolved organic carbon (DOC) concentration values that fall within/nearby the same class as the endmember, and NAIP aerial photographs. Evidence from those sources contributed to endmember-labeling with high confidence. However, lack of access to spectral libraries containing spectra of scene materials (e.g., oil; different combinations oil types, thicknesses, and/or states; vegetation; and/or water types/conditions) acquired at/near the time of sensor overpass may have lead to some endmember mislabeling. Endmember labeling is an important issue in this study, as all the labeled endmembers were used as input to the classification algorithms, affecting oil-vegetation detection efforts, hard classification images, and the accuracy assessments.

Classification accuracies for SID results are generally significantly lower than those for MESMA. However, for MTMF, classification accuracies across all AVIRIS images were significantly lower than those for SID and MESMA. The hard MTMF classification image exhibit marked differences in terms of misclassified pixels; this

issue may potentially at least partially be attributed to the nature of the classification input images used. The atmospherically- and geometrically-corrected AVIRIS images were used as input to SID and MESMA algorithms. However, the input data to MTMF was the output of the MNF transformed data. Therefore, the number of output MNF bands or the dimensionality-reduced information content could be insufficient for effective classification.

The results show that oiled dry marsh and light-oiled vegetation were successfully detected in the AVIRIS-based MESMA analysis, whereas these classes could not be accurately mapped in the SID and MTMF classifications. In terms of user's accuracies, the values for oiled dry marsh (68%) and light oiled vegetation (72%) were higher in the MESMA classification than the SID and MTMF and consistent across all AVIRIS images. However user's accuracies were much lower for oiled dry marsh (44%) and light oiled vegetation (48) particularly for the MTMF classification. The reason could potentially be explained by the ability of MESMA to test multiple endmember combinations and endmember spectra for each pixel in the image. Regarding the MESMA approach, 2-endmember and 3-endmember models were constructed and applied, and based on visual examination, the target classes were better identified in the hard classification image of the 2-endmember MESMA model rather than the 3-endmember model. When MESMA is applied to the AVIRIS data, oiled dry marsh and light-oiled vegetation are successfully discriminated. Accuracy-assessment results indicate that MESMA provides the most accurate hard classified images in terms of delineating oiled dry marsh, light-oiled vegetation and mixed (oil/water/vegetation)

classes. Besides, according to results of significance testing, there were statistically significant pairwise differences between multiple endmember classification algorithm, MESMA, and single endmember classification algorithms, SID and MTMF across all AVIRIS images with the exception of SID vs. MESMA for AVIRIS image 2. The oil classes were finely discriminated in Image 4. The heavy and medium oiled marsh vegetation classes were identified in addition to light oiled marsh vegetation, oiled dry marsh, mixed (oil/water/vegetation) and marsh vegetation classes. Therefore, for Image 4, the lower classification accuracies were acquired compare to Image 1, 2 and 3 due to larger number of classes and class specificity.

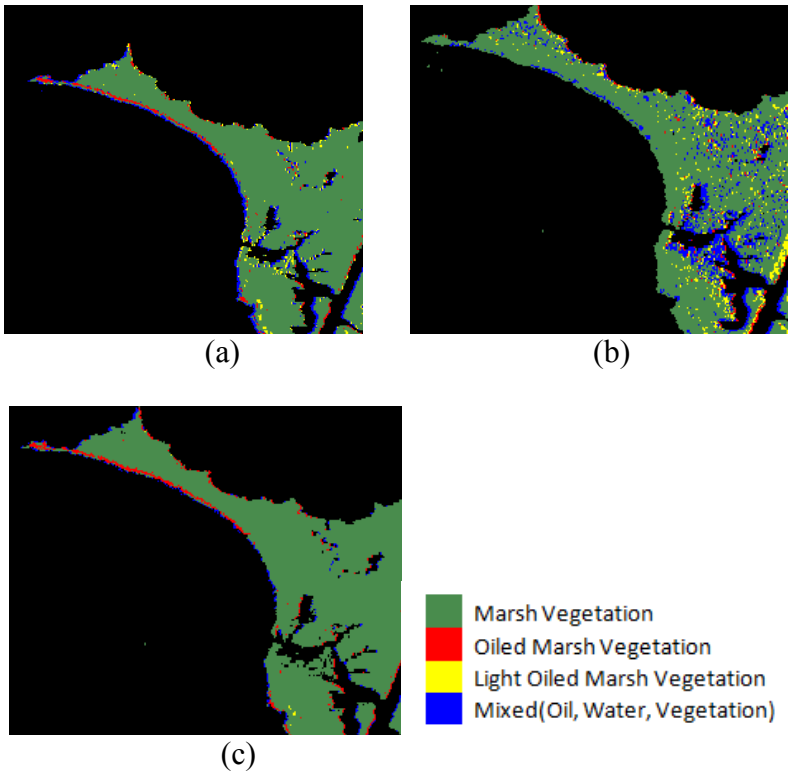

Figure 23 Hard classified zoom images for endmember-based classification approaches: a) SID; b) MTMF; and c) MESMA.

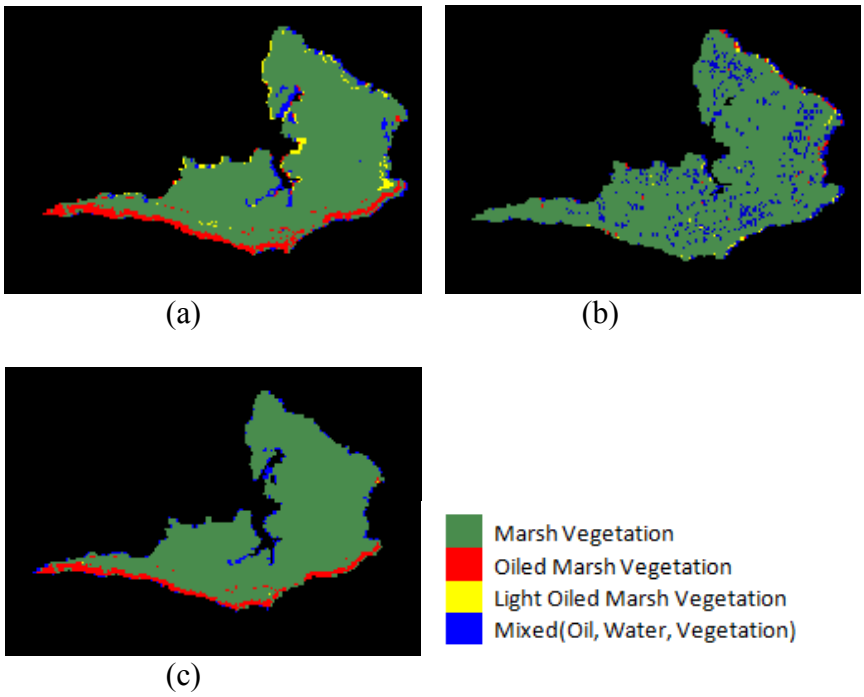

Figure 24 Hard classified zoom images for endmember-based classification approaches: a) SID; b) MTMF; and c) MESMA.

As shown in Figures 23 and 24, whereas oiled dry marsh, light-oiled vegetation and mixed (oil/water/vegetation) classes were accurately mapped across the SID and MESMA classifications, confusion among light-oiled vegetation, mixed (oil/water/vegetation) and marsh vegetation was observed in the MTMF results, as exhibited by the lower overall accuracy and Kappa coefficient, for example.

In this research, three sources of information were utilized as reference data in the construction of the error matrices: (1) SCAT oil map, which provides field-based observations of the degree of oil accumulation along the coastline; (2) high-spatial resolution NAIP aerial orthophotographs acquired before and after the oil spill; and (3) *in situ* measurements from the literature. An important factor in determining the

accuracy of a classification is the reference information used. The limited amount of ground-observed reference data may influence the assessed accuracies. The limited availability of spectral libraries is another restriction on the use of hyperspectral data and may lead to incorrect assumptions about the accuracy of a classification. Spectral libraries for differing oil thicknesses, different oil types and/or states, as well as combinations of these with spectra of various soils, water conditions, and vegetation species need to be developed in order to improve the performance of classification algorithms. In addition, the accuracy assessments were performed using 50 stratified random points per class. In order to perform a potentially more sensitive/representative accuracy assessment, a larger number of stratified random accuracy-assessment points could be generated. It should be noted though that maximally-useful field data could not be collected for the study area at the time at which this research was conducted due to the passage of time since the Deepwater Horizon spill and the associated changes in the amount, state, and distribution of oil within the site (as well as the uncertainties associated with these changes). Clean-up efforts—to the extent they may have existed in this area—may have also had some effect.

The persistence and distribution of oil within marshes depends on the vegetation species present and other factors (Stebbings, 1970). Thus, vegetation type within the study site likely plays an important role in determining the probability of oil existence at a given site. It is important to consider how the composition and concentration of oil are altered by weathering, including chemical, physical and biological processes. Due to degradation of oil in marsh vegetation over time, the chemical components of oil in such

an environment change over time, which in turn affects oil-reflectance features. Likewise, vegetation spectral features are also subject to critical changes due to physical and chemical effects of oil, which also has implications for detection of oil-impacted vegetation via remote sensing.

The distribution of oil on the sea surface occurs under the influence of wind, water current, tides and temperature. Currents, wind and warm temperatures typically cause oil to spread faster. The Gulf of Mexico is a dynamic, almost landlocked body of water dominated by prevailing southeast winds and influenced by the Gulf Loop Current and Mississippi River flow (The University of Texas Marine Science Institute, Marine Education Services, 2013). The prevailing winds in this area are from the south/southeast during the summer, and the prevailing wind flow during the cold season is from the northeast.

To assess oil distribution patterns on a localized scale as they relate to the classified images generated in this research, historical wind speed and wind direction data for Grand Isle station, which is the nearest weather station to the study site, were obtained from the NOAA National Data Buoy Center. The data set provides multiple records for each day in 2010. Since the AVIRIS images analyzed in this research were acquired on 14 September 2010, winds from the southeast with an average speed of ~4.03 m/s were the most frequent from the beginning of the oil spill to the AVIRIS and NAIP image-acquisition dates, although weaker winds from different directions were also common during the same time period. The extent of oil resulting from the Deepwater Horizon spill varied widely on a daily basis due to changes in wind patterns

and ocean currents. Previous studies have shown an uneven distribution of hydrocarbons over the surface of the Gulf of Mexico (Camilli *et al*., 2010; Diercks *et al*., 2010; Hazen *et al*., 2010; Kujawinski *et al*., 2011; Valentine *et al*., 2010). Surface oil advection is particularly sensitive to wind velocities, because their relative strength and onshore direction can push oil toward the marshes of southeastern Louisiana (Dietrich *et al*., 2012). Therefore, oil released from the Deepwater Horizon potentially migrated and spread quite far down the well head due to the influence of winds and currents. For instance, if the wind blows from southeast to northwest, which is the prevailing wind direction during the summer season, oil is more likely to be blown towards the Louisiana and Texas coasts. As an example, displayed in the Figure 25, the oiled dry marsh vegetation class was mapped along the southerly part of one of the islands in Barataria Bay by using MESMA and SID classification algorithms.

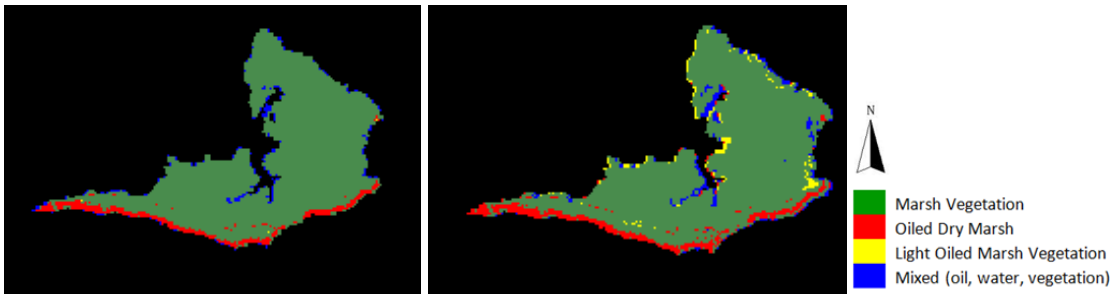

Figure 25 Hard classified images for the following endmember-based classification approaches: a) SID; and b) MESMA

Oil movement and distribution were likely affected by winds from the southeast/south during the summer; thus, oil was mostly accumulated along the southerly coastline. However, for coastlines of this island facing other directions, oiled

dry marsh vegetation or light-oiled marsh vegetation was rarely observed or not present in the AVIRIS-derived classified images or reference data. This example is for only one specific island; however, wind-driven processes likely affect the entire extents of the AVIRIS images. For instance, Dietrich *et al*. (2012) provide maps showing predicted and observed oil extents, including the wind vectors over the Gulf of Mexico (Figure 26). The map also depicts how wind vectors affect oil migration along the coastline of the Gulf of Mexico. Oil may not reach or significantly accumulate on the northerly part of the island noted above due to wind and current patterns. Therefore, the distribution of oil was probably affected by wind speed, wind direction, and water currents. This situation may explain the oil distribution within the Barataria Bay marshes.

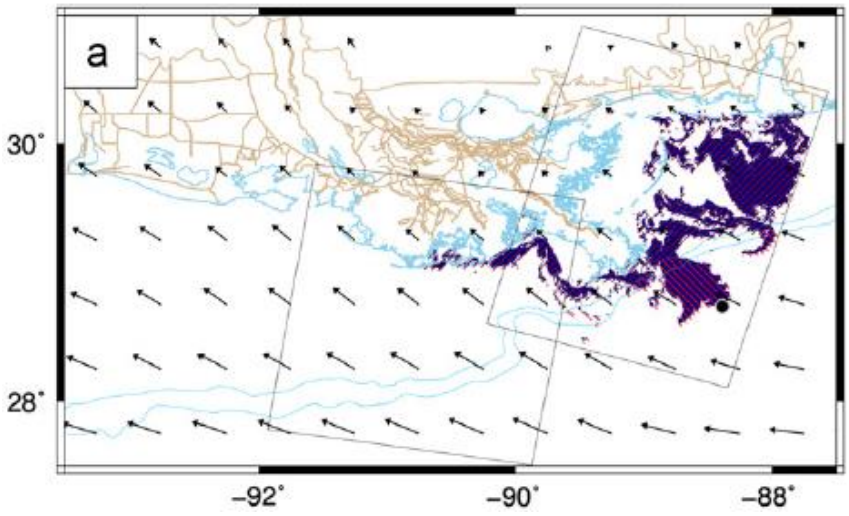

Figure 26 Comparison of observed (solid blue) and predicted (red hatched) oil extents during the mid-June time period along the coastline of the Gulf of Mexico (Dietrich *et al*., 2012)

In general, when an oil leak is occurring at the ocean floor, if a strong current has the same direction as the wind, it will increase the wind effect. When considering the spatial variability in the amount of oil accumulation at different sites within the study area of this research, it is important to understand the morphological characteristics of the coast, prevailing wind directions and speeds, and water currents. Wind history, along with information on ocean currents, is very useful in understanding oil-distribution behaviors (Espedal, 2010).

6.2 Conclusion

This research addresses remote sensing, especially hyperspectral image analyses of the Gulf of Mexico coastline. The area encompassing Barataria Bay is one of the heavy impacted areas by the BP Deepwater Horizon oil spill incident and this study was conducted to analyze and extract valuable information from airborne image data to detect and map oiled vegetation resulting from the Deepwater Horizon accident along the coastline of the Barataria Bay. This research has two objectives focused on AVIRIS data, the first objective was to detect oiled vegetation observed near the time frame of the Deepwater Horizon accident in the Gulf of Mexico coastal environment via SID and MTMF classification methods and the second objective was to detect oiled marsh vegetation over the same study site by performing MESMA approach which allows the number and type of endmembers to vary in each pixel of the image different than the

SID and MTMF. The overall objective of this study was to understand and compare the capability of MEMSA relative to SID and MTMF in detection of oiled vegetation.

In order to extract valuable information from hyperspectral images, the first task of this research study was the minimization of atmospheric effects by performing FLAASH atmospheric correction method. Image derived endmembers were extracted from the atmospherically and geometrically corrected hyperspectral AVIRIS data via MNF transform, PPI generation, and *n*-dimensional visualization. Extracted endmembers were then used as input to three different mapping algorithms; SID, MTMF and MESMA to yield fractional-abundance images and hard classification images. The overall accuracy, Kappa coefficient and Z Statistic were calculated in order to compare the performance of all classification algorithms. The classification results of MESMA algorithm performed much better than the SID and MTMF in detection of oiled vegetation along the coastline of the Bay Jimmy, Bay Chene Fleur, and Wilkinson Bay and in adjacent marshland area, with overall accuracies of 70-85%, and with Kappa coefficients of 0.7-0.8. All MESMA results yield significantly higher classification accuracies than MTMF and SID (at the 95% confidence level), (with the exception of SID vs. MESMA for Image 2), with Z statistics from the pairwise comparisons ranging between -1.8 to -9.0. MESMA and SID classification results are always significantly better than those of MTMF (at the 95% confidence level). For Image 4, lower classification accuracies were accrued (likely due to larger number of classes and class specificity); however, results for some algorithms are quite accurate given specificity of classes.

This research study contributes to debates on the effectiveness of AVIRIS data for the application of oil spill detection, and may suggest effective strategies for identifying oil spills in vegetated areas. In addition, this study entails importance in the case of an oil-spill accident; the methods and knowledge accrued here can be applied to formulate an effective environmental protection plan, and to reduce damage by predicting size and migration of oil. However, the major challenge of this study is the lack of spectral properties of oil spill in vegetated areas, therefore the spectral libraries of different oil amounts and combinations of oil with different soils, water and vegetation species need to be developed in order to improve the performance of classification algorithms. Another major challenge of this study is the limited amount of *in situ* data collected over the study area which is critical for an accuracy assessment, thus a large *in situ* database needs to be acquired to enhance the accuracy assessments process prior to oil spill detection and mapping studies for the future studies.

REFERENCES

Adams, J.B., Smith, M.O., & A.R. Gillespie (1993) Imaging spectroscopy: interpretation based on spectral mixture analysis*: in Remote geochemical analysis: Topics in Remote Sensing,* Cambridge University Press, Cambridge, England, pp. 145-166.

Akar, S., M. L. Süzen & N. Kaymakci (2011) Detection and object-based classification of offshore oil slicks uing ENVISAT-ASAR images. *Environmental Monitoring and Assessment,* 183**,** 409-423.

Boardman, J. W. (1998) Leveraging the high Dimensionality of AVIRIS data for improved sub-pixel target unmixing and rejection of false positives: mixture tuned matched filtering: in *Summaries of the 7th Annual JPL Airborne Geoscience Workshop*, JPL Publication 97-21, v. 1, p. 55.

Boardman, J. W., F. A. Kruse & R. O. Green. (1995) Mapping target signatures via partial unmixing of AVIRIS data. *Fifth JPL Airborne Earth Science Workshop*, 23-26.

Boardman J. W., and Kruse, F. A., (1994) Automated spectral analysis: A geologic example using AVIRIS data, north Grapevine Mountains, Nevada: in *Proceedings, Tenth Thematic Conference on Geologic Remote Sensing*, Environmental Research Institute of Michigan, Ann Arbor, MI, I-407 - I-418.

Boardman, J. W., (1993) Automated spectral unmixing of AVIRIS data using convex geometry concepts: in *Summaries, Fourth JPL Airborne Geoscience Workshop*, JPL Publication 93-26, v. 1, 11 - 14.

Boopathy, R., (2010) BP Oil Spill bioremediation in relation to oyster farming. Invited talk presented at the BOR's Conference on Collaborative Scientific Research Opportunities Relative to Gulf Oil Spill. Nov. 1-2, New Orleans, LA.

Brekke, C. & A. H. S. Solberg (2005) Oil spill detection by satellite remote sensing. *Remote Sensing of Environment,* 95**,** 1-13.

Campbell, J. (2007). Introduction to Remote Sensing (4th Edition) New York: The Guilford Press

Camilli, R., C. M. Reddy, D. R. Yoerger, B. A. S. Van Mooy, M. V. Jakuba, J. C. Kinsey, C. P. McIntyre, S. P. Sylva & J. V. Maloney (2010) Tracking hydrocarbon plume transport and biodegradation at Deepwater Horizon. *Science,* 330**,** 201-204.

Chein, I. C. & A. Plaza (2006) A fast iterative algorithm for implementation of pixel purity index. *Geoscience and Remote Sensing Letters, IEEE,* 3**,** 63-67.

Clark, R. N., J. M. Curchin, T. M. Hoefen & G. A. Swayze (2009) Reflectance spectroscopy of organic compounds: 1. Alkanes. *Journal of Geophysical Research: Planets,* 114**,** E03001.

Clark, R., G. Swayze, I. Leifer, K. Livo, R. Kokaly, T. Hoefen, S. Lundeen, M. Eastwood, O. Green, N. Pearson, C. Sarture, I. McCubbin, D. Roberts, E.Bradley, D. Steele, T. Ryan, & R. Dominguez (2010) A method for quantitative mapping of thick oil sills using imaging spectroscopy. *U.S. Geological Survey Open-File Report:* 1167.

Cloutis, E. A. (1989) Spectral reflectance properties of hydrocarbons: remote-sensing implications. *Science,* 245**,** 165-8.

Congalton, R. G. (1991) A review of assessing the accuracy of classifications of remotely sensed data. *Remote Sensing of Environment,* 37**,** 35-46.

Congalton, R. G. & K. Green, (2008) Assessing the Accuracy of Remotely Sensed Data Principles and Practices, (2nd Edition) CRC Press

Crone, T. J. & M. Tolstoy (2010) Magnitude of the 2010 Gulf of Mexico Oil Leak. *Science,* 330**,** 634.

Dennison, P. E. & D. A. Roberts (2003) Endmember selection for multiple endmember spectral mixture analysis using endmember average RMSE. *Remote Sensing of Environment,* 87**,** 123-135.

Dietrich, J. C., C. J. Trahan, M. T. Howard, J. G. Fleming, R. J. Weaver, S. Tanaka, L. Yu, R. A. Luettich Jr, C. N. Dawson, J. J. Westerink, G. Wells, A. Lu, K. Vega, A. Kubach, K. M. Dresback, R. L. Kolar, C. Kaiser & R. R. Twilley (2012) Surface trajectories of oil transport along the Northern Coastline of the Gulf of Mexico. *Continental Shelf Research,* 41**,** 17-47.

Drake, N. A., S. Mackin & J. J. Settle (1999) Mapping vegetation, soils, and geology in semiarid shrublands using spectral matching and mixture modeling of SWIR AVIRIS imagery. *Remote Sensing of Environment,* 68**,** 12-25.

Espedal, H. A. (1999) Satellite SAR oil spill detection using wind history information. *International Journal of Remote Sensing,* 20**,** 49-65.

Fingas, M. F. & C. E. Brown (1997) Review of oil spill remote sensing. *Spill Science & Technology Bulletin,* 4**,** 199-208.

FLAASH User's Guide, (2009) Atmospheric Correction Module Version 4.8

Franke, J., D. A. Roberts, K. Halligan & G. Menz (2009) Hierarchical multiple endmember spectral mixture analysis (MESMA) of hyperspectral imagery for urban environments. *Remote Sensing of Environment,* 113**,** 1712-1723.

Gaffey, S.J., L.A. McFadden, R. Nash, & C.M. Pieters (1993) Ultraviolet, visible, and near infrared spectroscopy: Laboratory spectra of geologic materials, Ch.3 in Remote Geochemical Analysis: Elemental and Mineralogical Composition. Cambridge University Press

Galloway, William E. (2009) Gulf of Mexico, *GEO Expro*, Issue 6, Volume 3.

Gambardella, A., M. Migliaccio & G. De Grandi (2007) Wavelet polarimetric SAR signature analysis of sea oil spills and look-alike features. In *Geoscience and Remote Sensing Symposium, 2007. IGARSS 2007. IEEE International*, 983-986.

Gilfillan, E. S., N. P. Maher, C. M. Krejsa, M. E. Lanphear, C. D. Ball, J. B. Meltzer & D. S. Page (1995) Use of remote sensing to document changes in marsh vegetation following the Amoco Cadiz oil spill (Brittany, France, 1978). *Marine Pollution Bulletin,* 30**,** 780-787.

Green, A. A., M. Berman, P. Switzer & M. D. Craig (1988) A transformation for ordering multispectral data in terms of image quality with implications for noise removal. *Geoscience and Remote Sensing, IEEE Transactions on,* 26**,** 65-74.

Green, R. O., M. L. Eastwood, C. M. Sarture, T. G. Chrien, M. Aronsson, B. J. Chippendale, J. A. Faust, B. E. Pavri, C. J. Chovit, M. Solis, M. R. Olah & O. Williams (1998) Imaging apectroscopy and the airborne visible/infrared imaging spectrometer (AVIRIS). *Remote Sensing of Environment,* 65**,** 227-248.

Hazen, T. C., E. A. Dubinsky, T. Z. DeSantis, G. L. Andersen, Y. M. Piceno, N. Singh, J. K. Jansson, A. Probst, S. E. Borglin, J. L. Fortney, W. T. Stringfellow, M. Bill, M. E. Conrad, L. M. Tom, K. L. Chavarria, T. R. Alusi, R. Lamendella, D. C. Joyner, C. Spier, J. Baelum, M. Auer, M. L. Zemla, R. Chakraborty, E. L. Sonnenthal, P. D'haeseleer, H.-Y. N. Holman, S. Osman, Z. Lu, J. D. Van Nostrand, Y. Deng, J. Zhou & O. U. Mason (2010) Deep-Sea oil plume enriches indigenous oil-degrading bacteria. *Science,* 330**,** 204-208.

Hirschfeld, T &A.Z. Hed, (1981) The atlas of near infrared spectra. Sadtler Research Laboratories.

Harsanyi, J. C. & I. C. Chein (1994) Hyperspectral image classification and dimensionality reduction: an orthogonal subspace projection approach. *Geoscience and Remote Sensing, IEEE Transactions on,* 32**,** 779-785.

Hu, C., F. E. Müller-Karger, C. Taylor, D. Myhre, B. Murch, A. L. Odriozola & G. Godoy (2003) MODIS detects oil spills in Lake Maracaibo, Venezuela. *Eos, Transactions American Geophysical Union,* 84**,** 313-319.

Hu, C. M., X. F. Li, W. G. Pichel & F. E. Muller-Karger (2009) Detection of natural oil slicks in the NW Gulf of Mexico using MODIS imagery. *Geophysical Research Letters,* 36.

Klemas, V. (2010) Tracking oil slicks and predicting their trajectories using remote sensors and models: Case studies of the Sea Princess and Deepwater Horizon Oil Spills. *Journal of Coastal Research***,** 789-797.

Kokaly, R. F., B. R. Couvillion, J. M. Holloway, D. A. Roberts, S. L. Ustin, S. H. Peterson, S. Khanna & S. C. Piazza (2013) Spectroscopic remote sensing of the distribution and persistence of oil from the Deepwater Horizon spill in Barataria Bay marshes. *Remote Sensing of Environment,* 129**,** 210-230.

Kullback, S. (1959) Information Theory and Statistics. New York: Wiley

Kujawinski, E. B., M. C. Kido Soule, D. L. Valentine, A. K. Boysen, K. Longnecker & M. C. Redmond (2011) Fate of dispersants associated with the Deepwater Horizon Oil Spill. *Environmental Science & Technology,* 45**,** 1298-1306.

Lammoglia, T. & C. R. d. S. Filho (2011) Spectroscopic characterization of oils yielded from Brazilian offshore basins: Potential applications of remote sensing. *Remote Sensing of Environment,* 115**,** 2525-2535.

Lee, J. B., A. S. Woodyatt & M. Berman (1990) Enhancement of high spectral resolution remote-sensing data by a noise-adjusted principal components transform. *Geoscience and Remote Sensing, IEEE Transactions on,* 28**,** 295-304.

Li, L., S. L. Ustin & M. Lay (2005) Application of AVIRIS data in detection of oil-induced vegetation stress and cover change at Jornada, New Mexico. *Remote Sensing of Environment,* 94**,** 1-16.

Lin, Q. & I. A. Mendelssohn (1996) A comparative investigation of the effects of south Louisiana crude oil on the vegetation of fresh, brackish and salt marshes. *Marine Pollution Bulletin,* 32**,** 202-209.

Liu, Y., Y. Shao, X. Qi, W. Tian & B. Wen (2009) Natural marine oil seepage detection and evaluation with SAR. 78411L-78411L-6.

Liu, T. & X. Yang (2013) Mapping vegetation in an urban area with stratified classification and multiple endmember spectral mixture analysis. *Remote Sensing of Environment,* 133**,** 251-264.

Matthew, M. W., S. M. Adler-Golden, A. Berk, S. C. Richtsmeier, R. Y. Levine, L. S. Bernstein, P. K. Acharya, G. P. Anderson, G. W. Felde, M. L. Hoke, A. J. Ratkowski, H.-h. K. Burke, R. D. Kaiser & D. P. Miller (2000). Status of atmospheric correction using a MODTRAN4-based algorithm. *Proc. SPIE* 4049, Algorithms for Multispectral, Hyperspectral, and Ultraspectral Imagery VI, 199-207.

Michel, J., Boring, C, Tarpley, J, Shigenaka, G. & Csulak, J, (2011) SCAT: Improving the process, training, tools, data management and products. *Proceedings International Oil Spill Conference,* Amer. Petr. Institute, Washington DC.

Michel, J., Owens, E. H., Zengel, S., Graham, A., Nixon, Z., Allard, T., Holton, W., Reimer, P. D., Lamarche, A., White, M., Rutherford, N., Childs, C.,Mauseth, G., Challenger, G., and & Taylor, E. (2013). Extent and degree of shoreline oiling: Deepwater Horizon Oil Spill, Gulf of Mexico, USA. *PloS one*, *8*(6).

Mishra, D. R., H. J. Cho, S. Ghosh, A. Fox, C. Downs, P. B. T. Merani, P. Kirui, N. Jackson & S. Mishra (2012) Post-spill state of the marsh: Remote estimation of the ecological impact of the Gulf of Mexico oil spill on Louisiana Salt Marshes. *Remote Sensing of Environment,* 118**,** 176-185.

National Commission on the BP Deepwater Horizon Oil Spill and Offshore Drilling. (2011) Deep water: the gulf oil disaster and the future of offshore drilling. Report to the President.

NOAA (2011) MC252 Shoreline Cleanup Assessment Technique (SCAT) Database, Emergency Response Division, Office of Response & Restoration. National Oceanographic and Atmospheric Administration, Seattle, WA.

Nirchio, F., M. Sorgente, A. Giancaspro, W. Biamino, E. Parisato, R. Ravera & P. Trivero (2005) Automatic detection of oil spills from SAR images. *International Journal of Remote Sensing,* 26**,** 1157-1174.

Owens, E.H., and Teal, A.R. (1990) Shoreline cleanup following the "Exxon Valdez" oil spill - field data collection within the SCAT program. *Proceedings 13th Arctic and Marine Oilspill Programme (AMOP) Technical Seminar*, Environment Canada, Edmonton, Alberta, 411-421.

Quintano, C., A. Fernández-Manso & D. A. Roberts (2013) Multiple Endmember Spectral Mixture Analysis (MESMA) to map burn severity levels from Landsat images in Mediterranean countries. *Remote Sensing of Environment,* 136**,** 76-88.

Painter, T. H., Roberts, D. A., Green, R. O. & Dozier, J. (1998) The effect of grain size on spectral mixture analysis of snow-covered area from AVIRIS data. *Remote Sensing of Environment*, 65, 320−332.

Pezeshki, S. R., M. W. Hester, Q. Lin & J. A. Nyman (2000) The effects of oil spill and clean-up on dominant US Gulf coast marsh macrophytes: a review. *Environmental Pollution,* 108**,** 129-139.

Ramsey Iii, E., A. Rangoonwala, Y. Suzuoki & C. E. Jones (2011) Oil Detection in a Coastal Marsh with Polarimetric Synthetic Aperture Radar (SAR). *Remote Sensing,* 3**,** 2630-2662.

Richards, J. A. (1993) Remote sensing digital image analysis: an introduction (2nd Edition), Berlin, Germany: Springer

Roberts, D. A., M. Gardner, R. Church, S. Ustin, G. Scheer & R. O. Green (1998) Mapping Chaparral in the Santa Monica Mountains using multiple endmember spectral mixture models - II. Environmental influences on regional abundance. *Remote Sensing of Environment,* 65**,** 267-279.

Roberts, D., K. Halligan & P. Dennison (2007) VIPER Tools User Manual, UC Santa Barbara, Department of Geography, Version 1.5, 1–91.

Salem, F., M. Kafatos, T. El-Ghazawi, R. Gomez & R. Yang (2005) Hyperspectral image assessment of oil-contaminated wetland. *International Journal of Remote Sensing,* 26**,** 811-821.

Salem, F. & Kafatos, M. (2001) Hyperspectral image analysis for oil spill detection. *22nd Asian Conference on Remote Sensing*, 5-9 Novermber, Singapore.

Salem, F., M. Kafatos, T. Ghazawi, R. Gomez, & R. Yang (2004) Hyperspectral image analysis for oil spill detection. *IEEE Transactions on Geoscience and Remote Sensing* 30: 496-507.

Sammarco, P. W., S. R. Kolian, R. A. F. Warby, J. L. Bouldin, W. A. Subra & S. A. Porter (2013) Distribution and concentrations of petroleum hydrocarbons associated with the BP/Deepwater Horizon Oil Spill, Gulf of Mexico. *Marine Pollution Bulletin,* 73**,** 129-143.

Smith, M.O. & J.B. Adams (1985) Interpretation of AIS images of Cuprite, Nevada using constraints of spectral mixtures Proceedings, AIS Workshop, JPL Publication 85-41, Pasadena, CA, 8–10 April, pp. 62–67.

Shu, Y., J. Li, H. Yousif & G. Gomes (2010) Dark-spot detection from SAR intensity imagery with spatial density thresholding for oil-spill monitoring. *Remote Sensing of Environment,* 114**,** 2026-2035.

Stebbings, R. E. (1970). Recovery of salt marsh in Brittany sixteen months after heavy pollution by oil. *Environmental Pollution (1970)*, *1*(2), 163-167.

The University of Texas Marine Science Institute, Marine Education Services, (2013) http://www.utmsi.utexas.edu/beach_debris [date last accessed: 15 October 2013].

Thorp, K. R., A. N. French & A. Rango (2013) Effect of image spatial and spectral characteristics on mapping semi-arid rangeland vegetation using multiple endmember spectral mixture analysis (MESMA). *Remote Sensing of Environment,* 132**,** 120-130.

van der Meer, F. (2006) The effectiveness of spectral similarity measures for the analysis of hyperspectral imagery. *International Journal of Applied Earth Observation and Geoinformation,* 8**,** 3-17.

Valentine, D. L., J. D. Kessler, M. C. Redmond, S. D. Mendes, M. B. Heintz, C. Farwell, L. Hu, F. S. Kinnaman, S. Yvon-Lewis, M. Du, E. W. Chan, F. G. Tigreros & C. J. Villanueva (2010) Propane respiration jump-starts microbial response to a deep oil spill. *Science,* 330**,** 208-211.

Vega, F. A., E. F. Covelo, M. J. Reigosa & M. L. Andrade (2009) Degradation of fuel oil in salt marsh soils affected by the Prestige oil spill. *Journal of Hazardous Materials,* 166**,** 1020-1029.